High energy hadron production Monte Carlo codes

J.Ranft, Siegen University, Germany

J.R., (and D.Heck,Karlsruhe for the Section on model comparisons)

(1) Introduction

(2) Quantum molecular dynamics models (QMD)

(3) DPM and QGSM models

(4) RHIC data and DPM–models

(5) Model comparisons (Cosmic ray experiment oriented)

(6) Conclusions

(2) Quantum molecular dynamics models (QMD)

(*) QMD: non–relativistic models $E < 2AGeV$ not treated here

(*) RQMD: first relativistic model H. Sorge not supported since 2000 ,used in FLUKA for A–A collisions below 5AGeV

(*) UrQMD: relativistic model Bass et al (Stöcker group in Frankfurt), Used in COSIKA Cosmic Ray cascade code below 80AGeV

(*) FLUKA efforts not treated here:

(1) F.Cerutti et al. add (approximate) energy conservation, evaporation, and residual nuclei to RQMD

(2) M.V.Garzelli et al. low enery QMD for A–A collisions in FLUKA

(3) Milano and Houston full relativistic model for A–A collisions in FLUKA under construction

(2.2) Relativistic QMD models

Lorentz invariant cascade (molecular dynamics) with nucleons of both nuclei and all produced hadrons as participants

Formation zone of all produced hadrons

Elementary interactions:
(1) h + h $\longrightarrow$ resonance; resonance + resonance and resonance decay (similar to HADRIN in FLUKA)
(2) high enery: h + h $\longrightarrow$ hadronic chain; 2 hadronic chains and Lund like chain fragmentation
(3) Chain fusion (called formation of color ropes) in RQMD
(4) Empirical parametrization of all cross sections
(5) pQCD description of hard collisions (UrQMD)

The kinematics of the models, (UrQMD)

The model is based on covariant propagation of all hadrons on classical trajectories in combination with stochastic binary scatterings, color string formation and resonance decay.

MC solution of a set of coupled partial integro-differential equ.
Each nucleon represented by a coherent state ($\hbar, c = 1$)

$$\phi_i(\vec{x}; \vec{q}_i, \vec{p}_i, t) = \left(\frac{2}{L\pi}\right)^{3/4} \exp\left\{-\frac{2}{L}(\vec{x} - \vec{q}_i(t))^2 + \frac{1}{\hbar} \mathrm{i} \vec{p}_i(t)\vec{x}\right\} \quad (1)$$

characterized by 6 time-dependent parameters, $\vec{q}_i$ and $\vec{p}_i$.
L, (extension of the wave packet in phase space), fixed.
Total n-body wave function: product of coherent states (**??**)

$$\Phi = \prod_i \phi_i(\vec{x}, \vec{q}_i, \vec{p}_i, t) \quad (2)$$

The Hamiltonian H of the system contains a kinetic term and mutual interactions V_{ij} $(H = \sum_i T_i + \frac{1}{2}\sum_{ij} V_{ij})$. This yields an Euler-Lagrange equation for each parameter.

$$\dot{\vec{p}}_i = -\frac{\partial \langle H \rangle}{\partial \vec{q}_i} \quad \text{and} \quad \dot{\vec{q}}_i = \frac{\partial \langle H \rangle}{\partial \vec{p}_i}\,. \tag{3}$$

$$\dot{\vec{q}}_i = \frac{\vec{p}_i}{m} + \nabla_{\vec{p}_i} \sum_j \langle V_{ij} \rangle = \nabla_{\vec{p}_i} \langle H \rangle \tag{4}$$

$$\dot{\vec{p}}_i = -\nabla_{\vec{q}_i} \sum_{j \neq i} \langle V_{ij} \rangle = -\nabla_{\vec{q}_i} \langle H \rangle \tag{5}$$

$$\langle V_{ij} \rangle = \int d^3x_1\, d^3x_2\, \phi_i^* \phi_j^* V(x_1, x_2) \phi_i \phi_j \tag{6}$$

These are the time evolution equations which are solved numerically.

UrQMD Hamiltonian: $E_{kin}, E_{jk}^{Sk2}, E_{jkl}^{Sk3}, E_{jk}^{Yukawa}, E_{jk}^{Coulomb}, E_{jk}^{Pauli}$

UrQMD: not really Lorentz invariant MD.

Authors: time order of individual binary collisions strongly varies with the reference frame.

S–S collisions: multiplicities and collision numbers vary by 3% between lab and CM frame.

RQMD: manifestly Lorentz invariant eq. of motion

Using 4–vectors for positions and momenta

Each particle carries its own time

2N add. degrees of freedom fixed by 2N constraints

N mass shell constraints: $H_i = p_i^2 - m_i^2 - V_i = 0$,

V_i: quasi potential

(N-1) time fixations

2Nth: relation of times of particles to eolution parameter τ

Projectile or target nucleus modeled according to Fermi-gas ansatz.
Wave-function of the nucleus: product wave-function.
Centroids of the Gaussians randomly distributed within sphere with radius $R(A)$,

$$R(A) = r_0 \left(\frac{1}{2} \left[A + \left(A^{\frac{1}{3}} - 1 \right)^3 \right] \right)^{\frac{1}{3}} \qquad r_0 = \left(\frac{3}{4\pi\rho_0} \right)^{\frac{1}{3}} . \tag{7}$$

ρ_0: the nuclear matter ground state density.
The phase-space density at the location of each nucleon: If too high (i.e. area of the nucleus already occupied), then location of that nucleon rejected and new location randomly chosen.
Initial momenta of the nucleons: randomly chosen between 0 and the local Thomas-Fermi-momentum:

$$p_F^{max} = \hbar c \left(3\pi^2 \rho \right)^{\frac{1}{3}} , \tag{8}$$

with ρ being the corresponding local proton- or neutron-density.

Disadvantage of this type of initialization: initialized nuclei not in their ground-state with respect to the Hamiltonian used for the propagation.
The parameters of the Hamiltonian: tuned to the equation of state of infinite nuclear matter and to properties of finite nuclei (such as their binding energy and their root mean square radius).
One can use a so-called Pauli-Potential in the Hamiltonian: Advantage: initialized nuclei remain absolutely stable whereas in the conventional initialization and propagation without the Pauli-Potential the nuclei start evaporating single nucleons after approximately 20 - 30 fm/c.
Drawback of the potential: the kinetic momenta of the nucleons are not anymore equivalent to their canonic momenta, i.e. the nucleons carry the correct Fermi-momentum, but their velocity is zero.

Impact parameter of a collision: sampled according to the quadratic measure $(dW \sim bdb)$.

At given impact parameter centers of projectile and target are placed along the collision axis in such a manner that a distance between surfaces of the projectile and the target is equal to 3 fm.

Momenta of nucleons: transformed into the system where the projectile and target have equal velocities directed in different directions of the axis.
After that the time propagation starts. During the calculation each particle is checked at the beginning of each time step whether it will collide within that time step.

(2.3) RQMD, UrQMD comparison to data

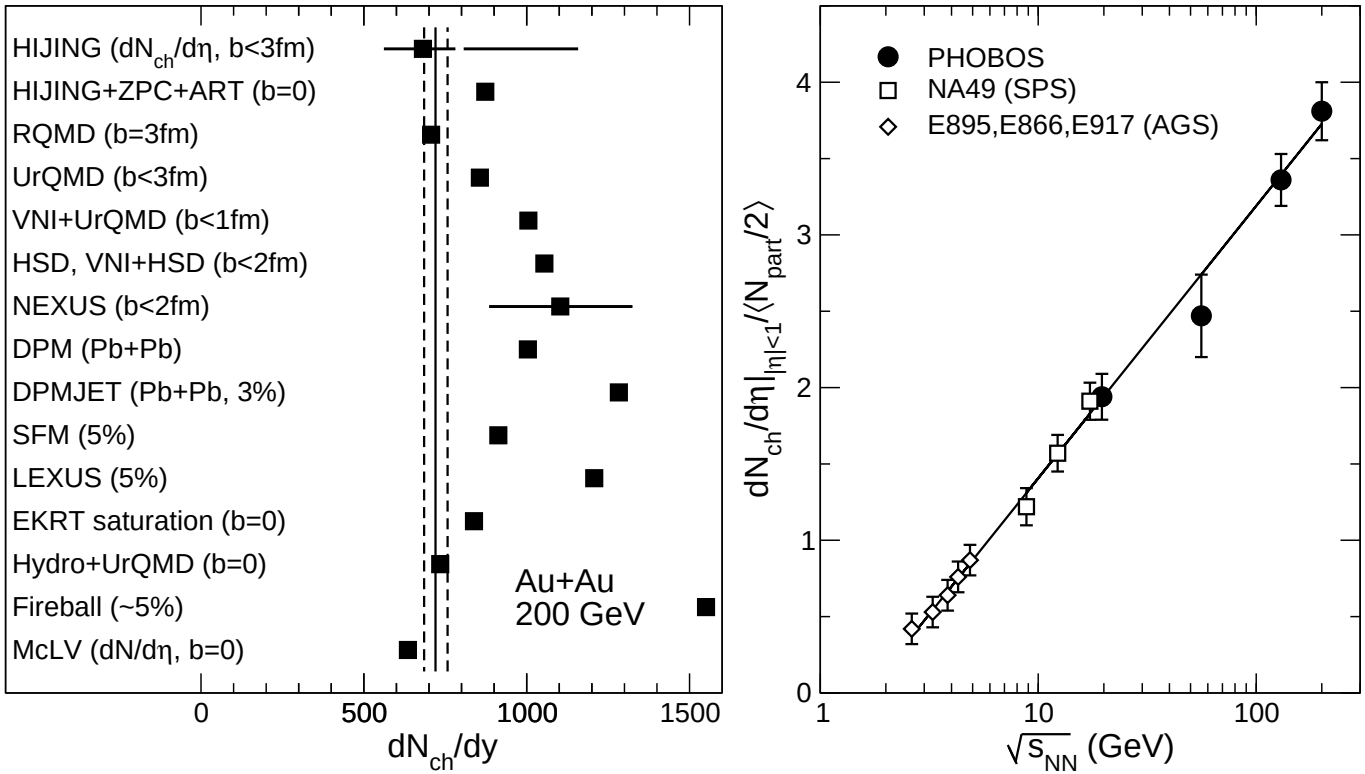

RHIC collaborations compare their results with RQMD

RQMD results in PHOBOS white paper

Chain fusion in RQMD: agreement with PHOBOS dN_{ch}/dy

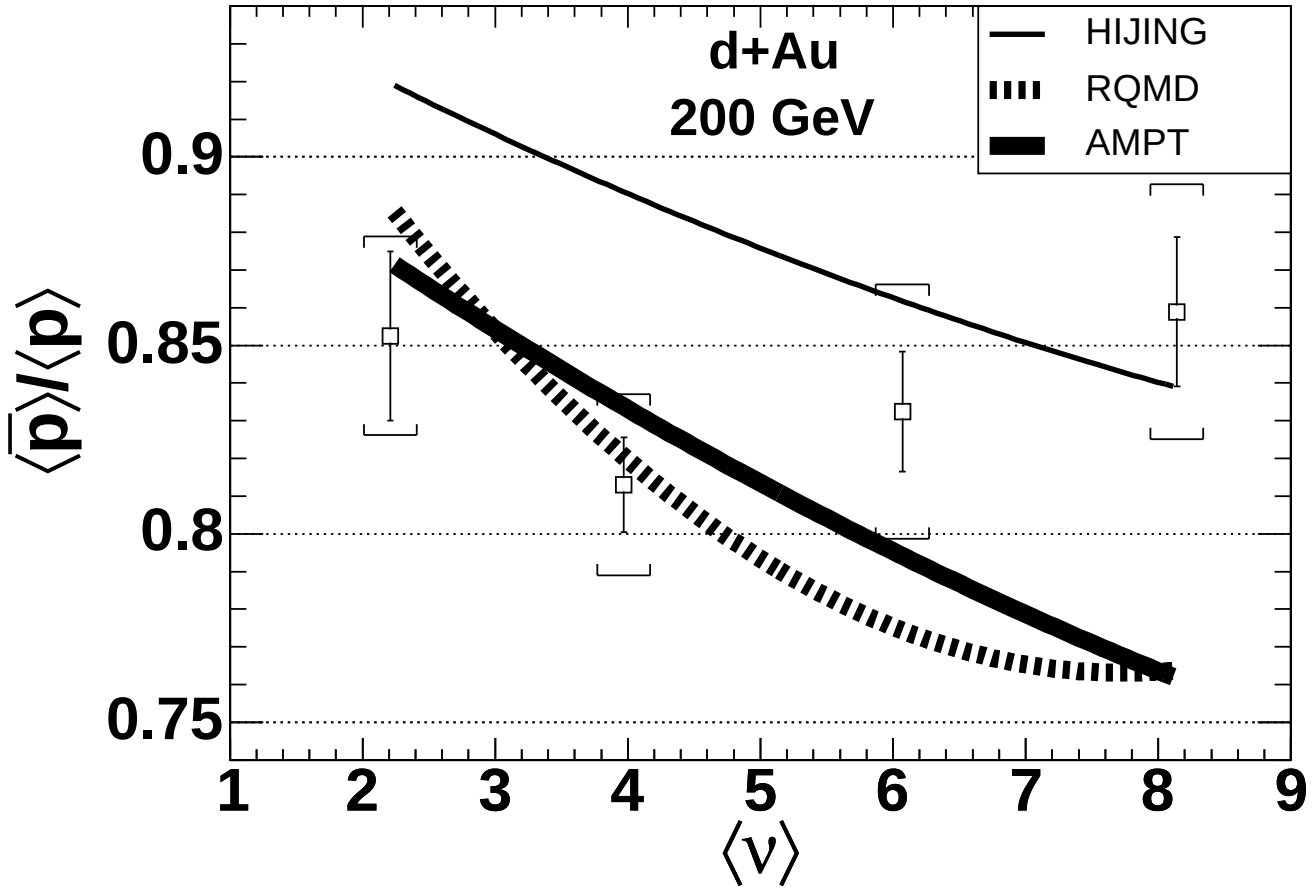

RQMD results in PHOBOS white paper

RQMD disagrees to centrality dependence of d–Au $< \bar{p} > / < p >$

Basic Checks (II)

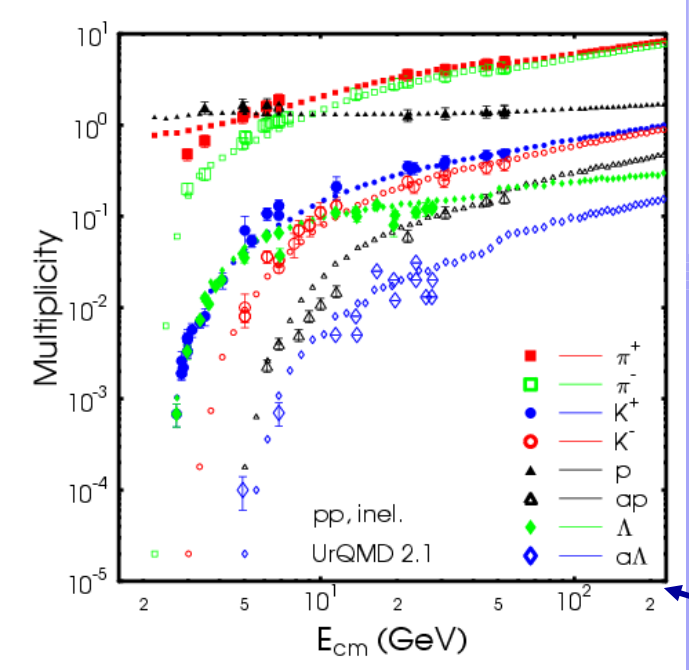

Unfortunately the data has poor quality

One has to rely on the extrapolation

This leads to ~10% systematic uncertainty

E=21000 AGeV

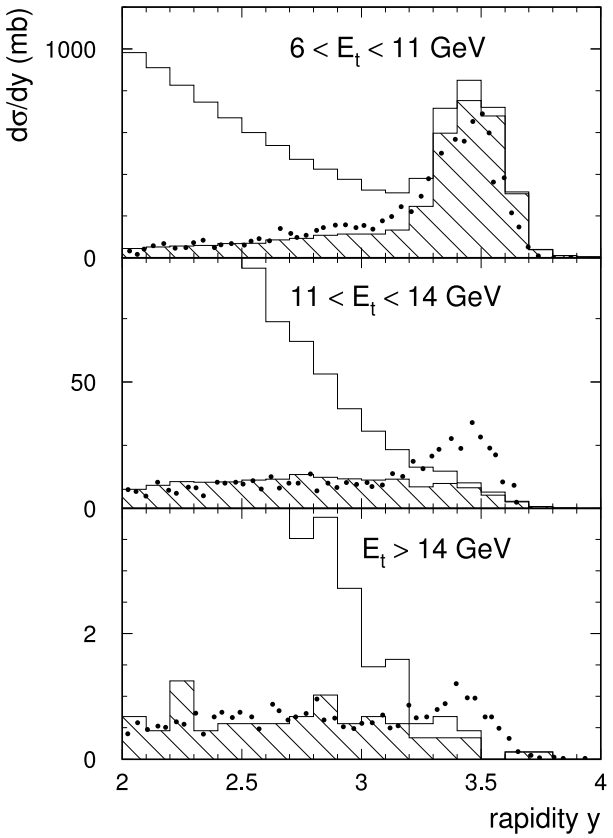

Ding et al. Comparison of E814 data Si–Pb at 14.6 AGeV with UrQMD

dN/dy for p and n with $p_\perp \leq$ 0.3 GeV in different $E_\perp$ bins.

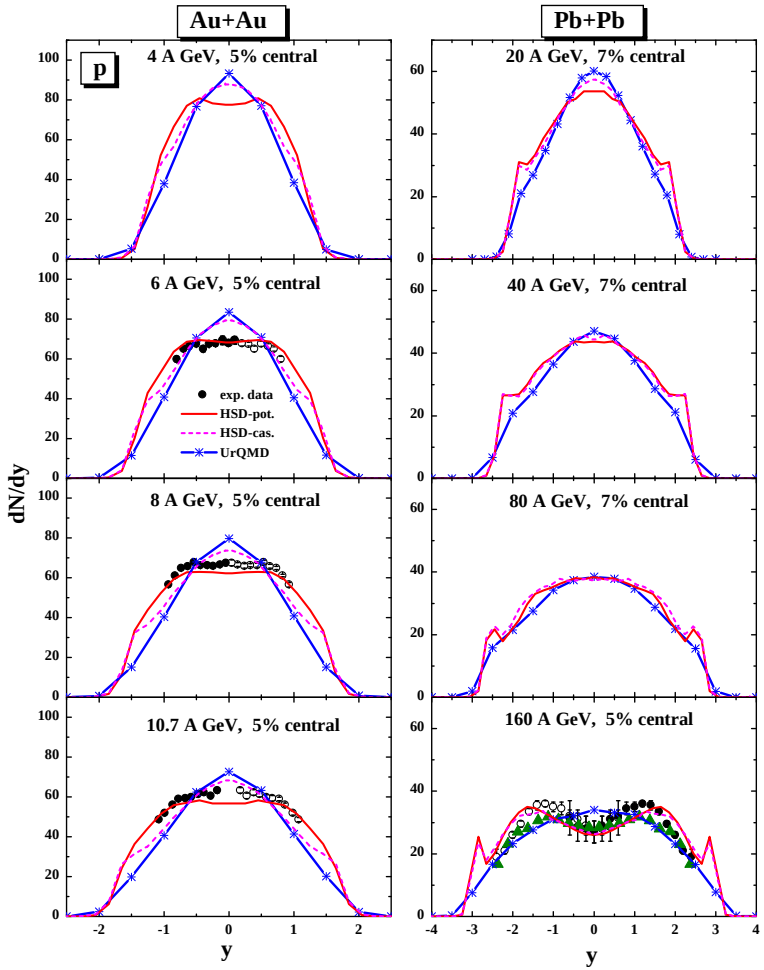

Weber et al. Frankfurt, dN/dy of protons, 5% Au–Au collisions (AGS) and Pb–Pb (SPS) at different energies, Symbols: data, blue lines: UrQMD. Too much stopping in UrQMD.

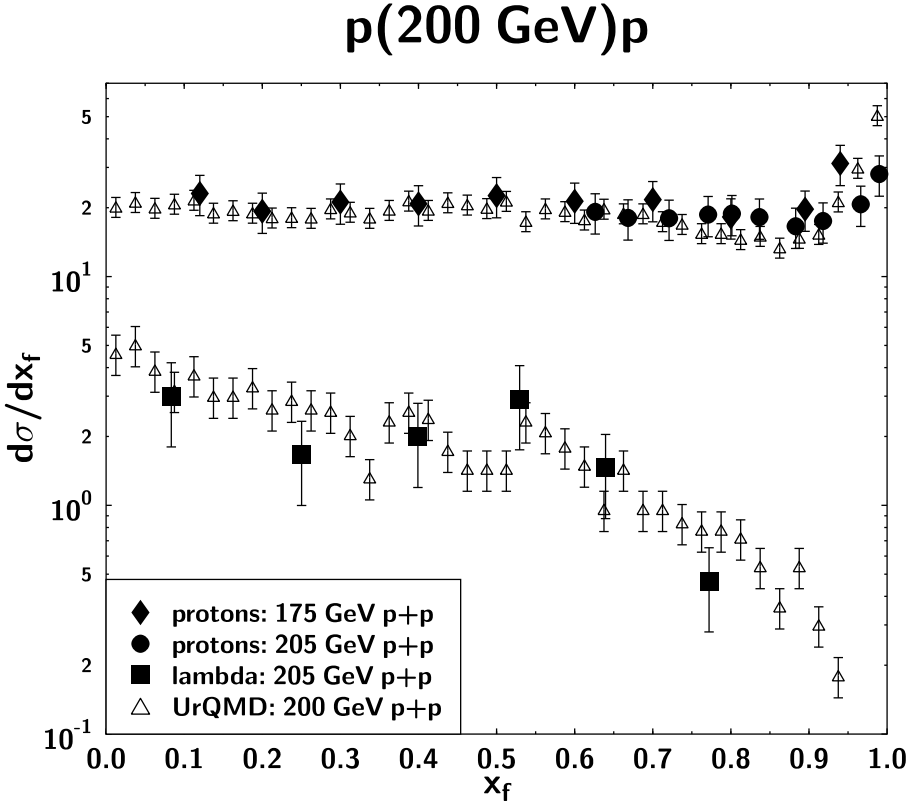

Bass et al. Frankfurt: x_F distributions of Λ and p in p–p collisions at 200 GeV, data and UrQMD

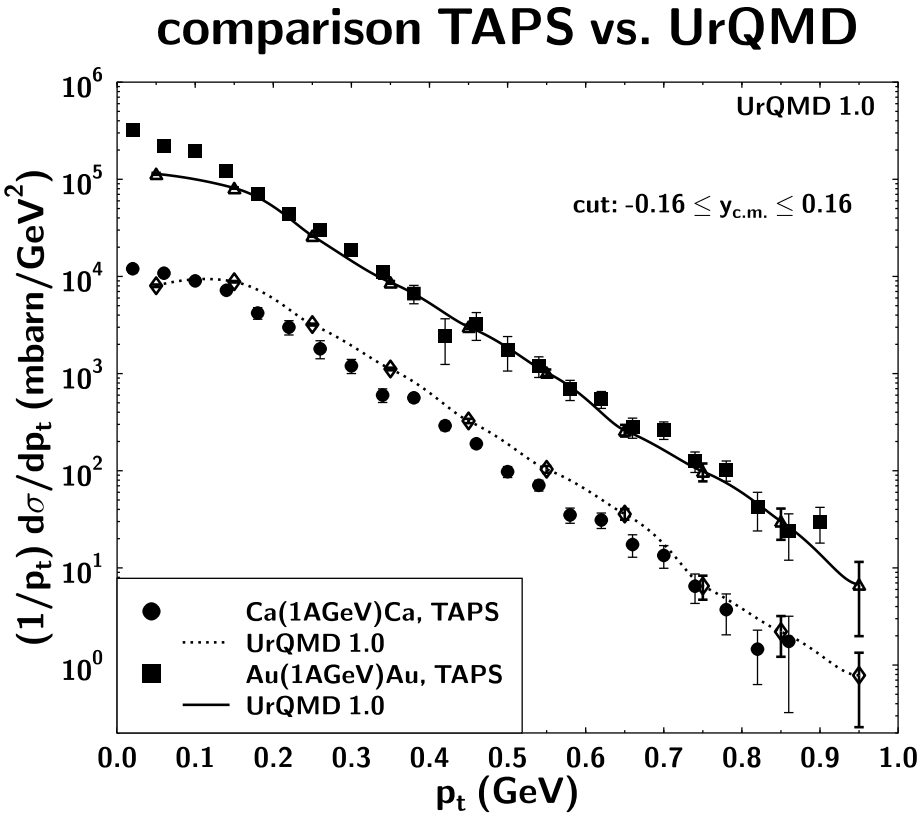

Bass et al. Frankfurt: $p_\perp$ distributions in min.bias Au–Au and Ca–Ca collisios, 1AGeV, TAPS data compared to UrQMD

(3) DPM and QGSM models

Two models, largely equivalent in their construction, but with characteristic differences:

Dual Parton Model DPM

Quark Gluon String Model QGSM

DPM due to Capella and Tran Than Van and collaborators

Monte Carlo models: PHOJET, h–h and γ–h collisions; DPMJET, h–A, A–A and γ–A collisions; Authors: Engel, Ranft and Roesler and collaborators

QGSM due to Kaidalov, Ter-Martyrosian and collaborators

Monte Carlo models: QGSJET, h–h, h–A and A–A collisions; Authors: Kalmykov, Ostapchenko and collaborators

(3.2) The construction of the PHOJET multichain model

We restrict us in this contribution to describe the PHOJET model, which is used directly for h–h collisions and for all elementary Glauber collisions in h–A and A–A collisions in DPMJET . There are no essential differnces in the formulation of the Glauber model between the Monte Carlo models

The (soft) Born cross section of the supercritical pomeron has the form

$$\sigma_s = g^2 s^{\alpha(0)-1}. \tag{9}$$

The supercritical pomeron has $\alpha(0) > 1.$, therefore (**??**) clearly violates unitarity.

According to the Froissart bound the cross section asymptotically should not rise faster than $(\log s)^2$.

If we start to construct the full model, which is unitarized, we should introduce some more input Born cross sections.

The hard cross section, which we calculate according to the QCD improved parton model

$$\sigma^{\text{hard}}(s, p_\perp^{\text{cutoff}}) = \int dx_1 dx_2 d\hat{t} \sum_{i,j,k,l} \frac{1}{1+\delta_{k,l}}$$

$$f_{a,i}(x_1, Q^2) f_{b,j}(x_2, Q^2) \frac{d\sigma^{\text{QCD}}_{i,j\to k,l}(\hat{s}, \hat{t})}{d\hat{t}} \Theta(p_\perp - p_\perp^{\text{cutoff}}), \qquad (10)$$

where $f_{a,i}(x_1, Q^2)$ is the distribution of the parton i in a.

Difference between PHOJET/DPMJET and QGSJET: $p_\perp^{\text{cutoff}}$

PHOJET/DPMJET:$p_\perp^{\text{cutoff}}$ rising with energy

QGSJET:$p_\perp^{\text{cutoff}}$ constant

We introduce furthermore the cross sections for high–mass single and double diffraction σ_D and for high–mass central diffraction σ_C according to the standard expressions.

The amplitudes corresponding to the one-pomeron exchange are unitarized applying an eikonal formalism

In impact parameter representation, the eikonalized scattering amplitude has the structure

$$a(s,B) = \frac{i}{2}\left(\frac{e^2}{f_{q\bar{q}}^2}\right)^2 \left(1 - e^{-\chi(s,B)}\right) \tag{11}$$

with the eikonal function

$$\chi(s,B) = \chi_S(s,B) + \chi_H(s,B) + \chi_D(s,B) + \chi_C(s,B). \tag{12}$$

Here, $\chi_i(s,B)$ denotes the contributions from the different Born graphs: (S) soft part of the pomeron and reggeon, (H) hard part of the pomeron (D) triple- and loop-pomeron, (C) double-pomeron graphs.

The eikonals $\chi_i(s,B)$ are defined as follows

$$\chi_i(s,B) = \frac{\sigma_i(s)}{8\pi b_i}\exp[-\frac{B^2}{4b_i}]. \tag{13}$$

The free parameters are fixed by a global fit to proton-proton cross sections and elastic slope parameters.

Once the free parameters are determined, the probabilities for the different final state configurations are calculated from the discontinuity of the elastic scattering amplitude (optical theorem).

The total discontinuity can be expressed as a sum of graphs with k_c soft pomeron cuts, l_c hard pomeron cuts, m_c triple- or loop-pomeron cuts, and n_c double-pomeron cuts by applying the Abramovski-Gribov-Kancheli cutting rules .

In impact parameter space one gets for the inelastic cross section

$$\sigma(k_c, l_c, m_c, n_c, s, B) = \frac{(2\chi_S)^{k_c}}{k_c!}\frac{(2\chi_H)^{l_c}}{l_c!}\frac{(2\chi_D)^{m_c}}{m_c!}\frac{(2\chi_C)^{n_c}}{n_c!}\exp[-2\chi(s,B)] \tag{14}$$

with

$$\int d^2B \sum_{k_c+l_c+m_c+n_c=1}^{\infty} \sigma(k_c, l_c, m_c, n_c, s, B) \approx \sigma_{\text{tot}} \qquad (15)$$

where σ_{tot} denote the total cross section

In the Monte Carlo realization of the model, the different final state configurations are sampled from Eq. (**??**).

For pomeron cuts involving a hard scattering, the complete parton kinematics and flavors/colours are sampled according to the Parton Model.

For pomeron cuts without hard large momentum transfer, the partonic interpretation of the Dual Parton Model is used: mesons

are split into a quark-antiquark pair whereas baryons are approximated by a quark-diquark pair.

The longitudinal momentum fractions of the partons are given by Regge asymptotics . We give it here for an event with n_s soft and $n_h (n_h \geq 1)$ hard cut pomerons, sea–quarks are used at the chain ends if we have more than one soft pomeron.

$$\rho(x_1, ..., x_{2n_s}, ..., x_{2n_s+2+n_h}) \sim \frac{1}{\sqrt{x_1}} \left(\prod_{i=3}^{2n_s+2} \frac{1}{x_i} \right) x_2^{1.5} \prod_{i=2n_s+3}^{2n_s+2+n_h} g(x_i, Q_i) \delta\left(1 - \sum_{i=1}^{2n_s+2+n_h} x_i\right). \quad (16)$$

The distributions $g(x_i, Q_i)$ are the distribution functions of the partons engaged in the hard scattering. The momentum fractions of the constituents at the ends of the different chains are sampled from this exclusive parton distribution,

After all this we we have all chains defined and PHOJET/DPMJET continues with hadronizing all multiple chains using the Lund code JETSET (PYTHIA).

Now we are able to compare the multichain model Phojet with particle production data.

(3.3) Comparison to data

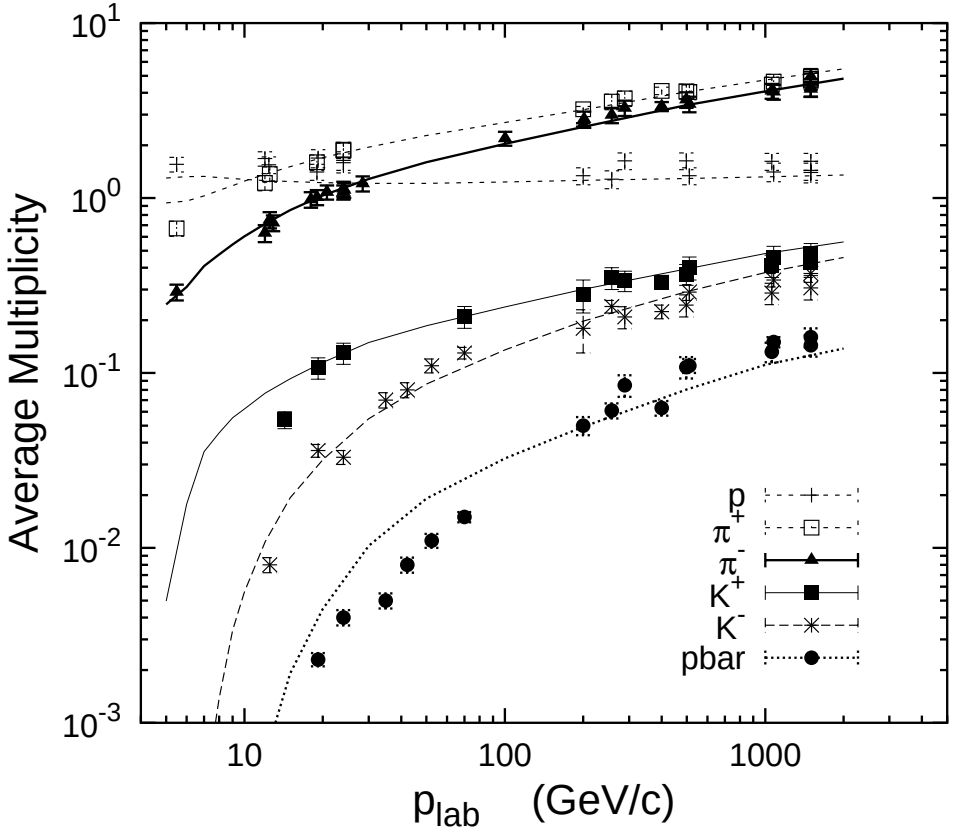

Average particle multiplicity proton-proton interactions. Phojet results (curves) are compared to experimental data (symbols).

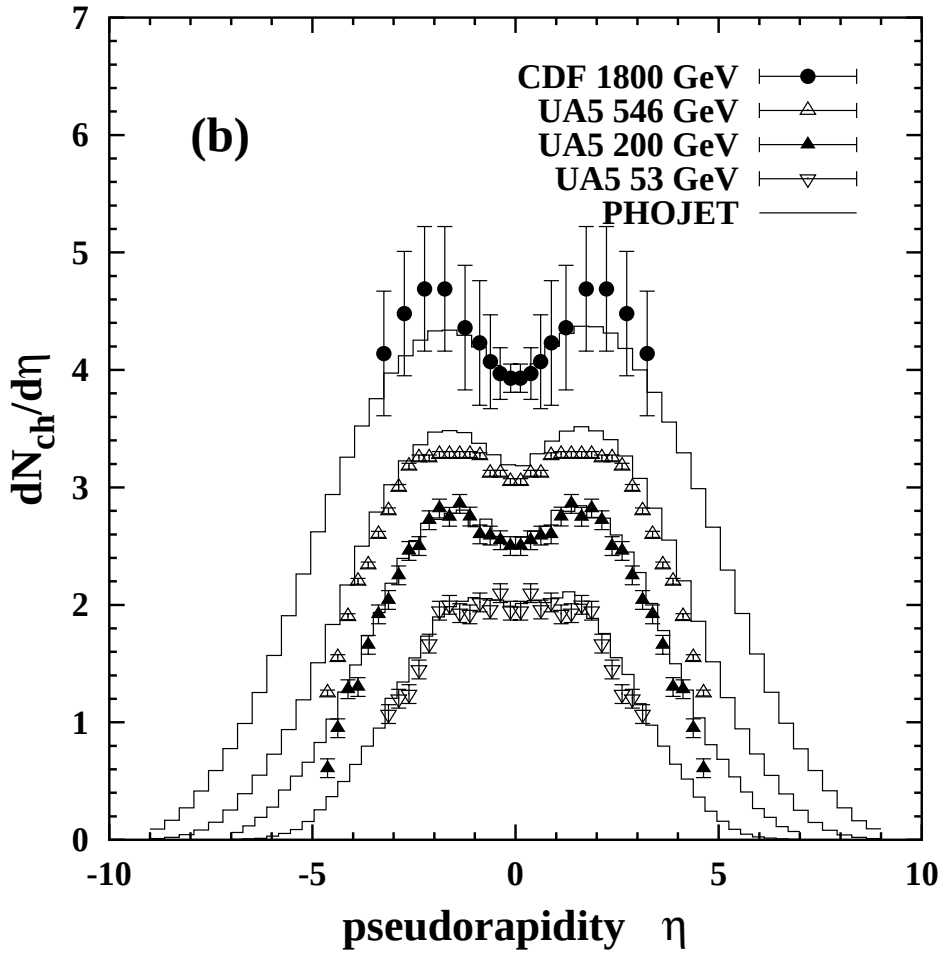

Energy-dependence of charged particle pseudorapidity density in $p\bar{p}$ collisions. phojet is compared to data from different colliders

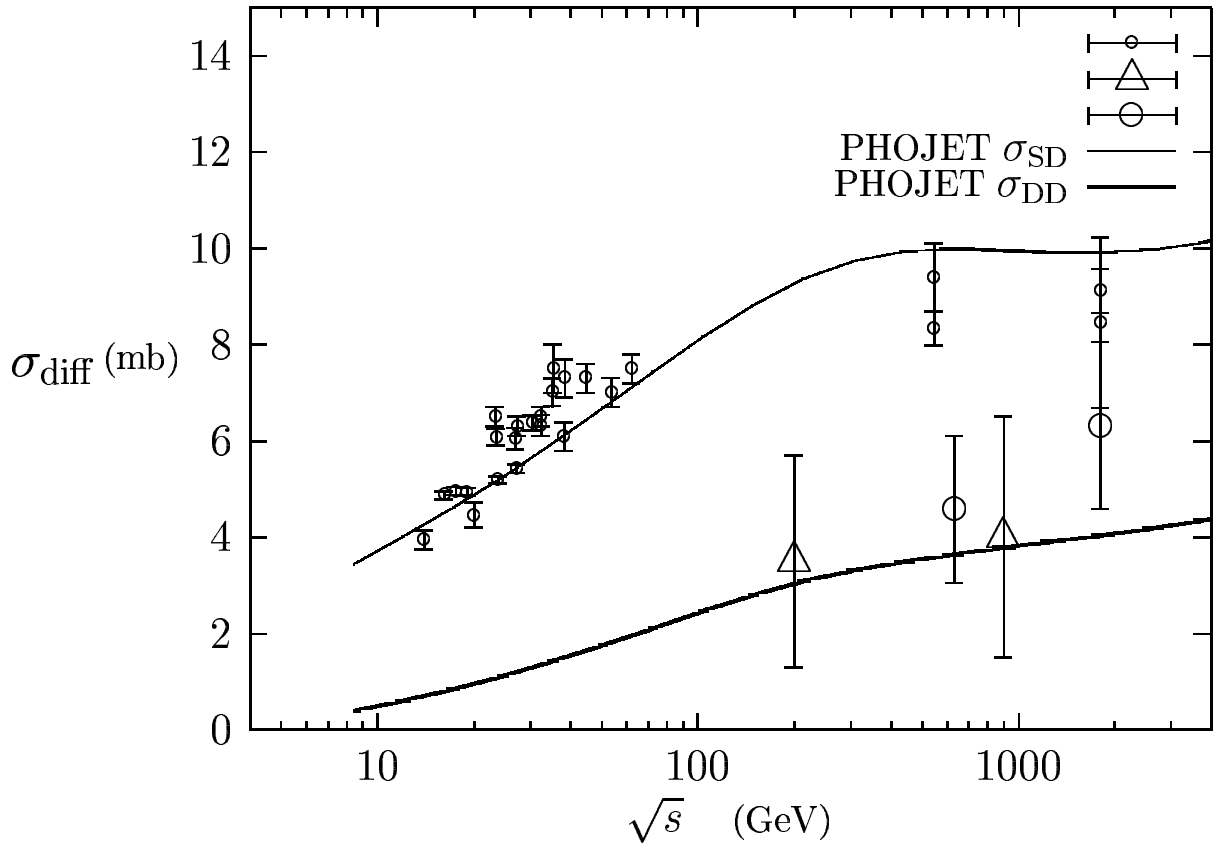

Single diffractive cross–sections σ_{SD} and double diffractive cross–sections σ_{DD} in pp and $p\bar{p}$ collisions. The Phojet results are compared with experimental data. The experimental data in single diffraction are taken from a summary of Goulianos. The data on double diffraction contain CDF data .

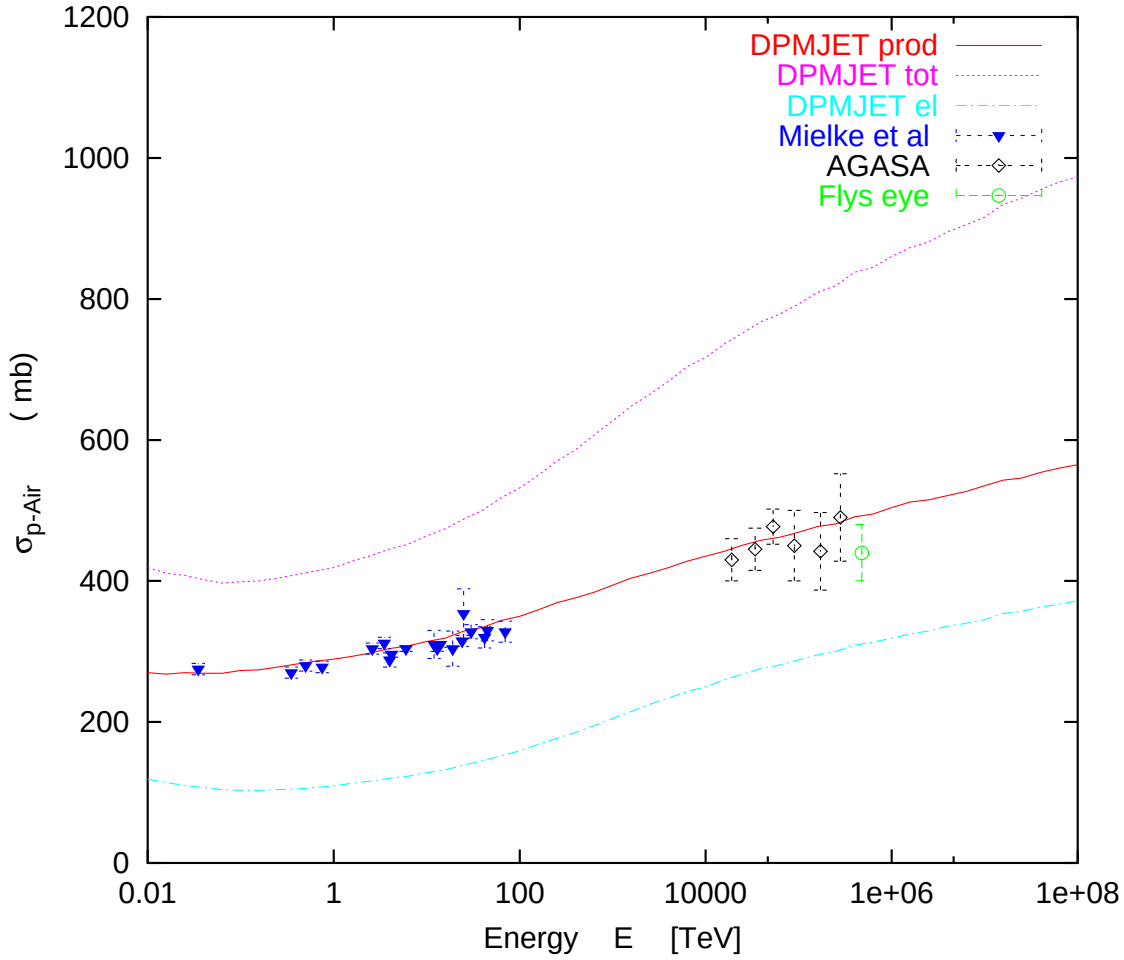

The inelastic cross section σ_{p-Air} calculated by Dpmjet as function of the laboratory energy E compared to experimental data collected by Mielke et al. and from AGASA and Fly's eye.

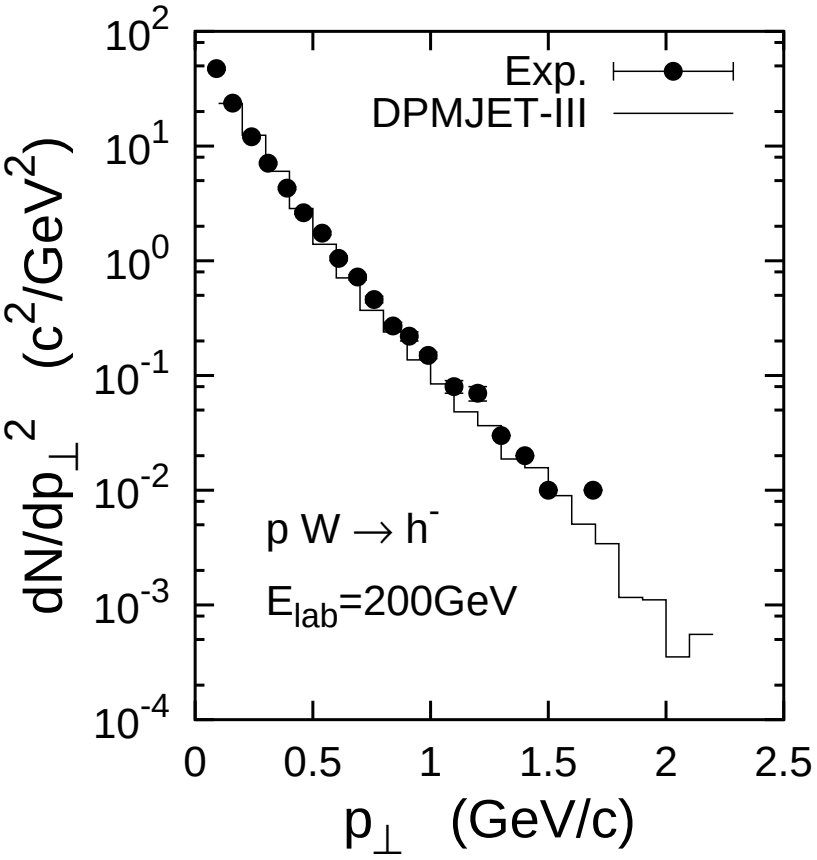

Transverse momentum distribution of negative hadrons in proton-tungsten collisions at 200 GeV.

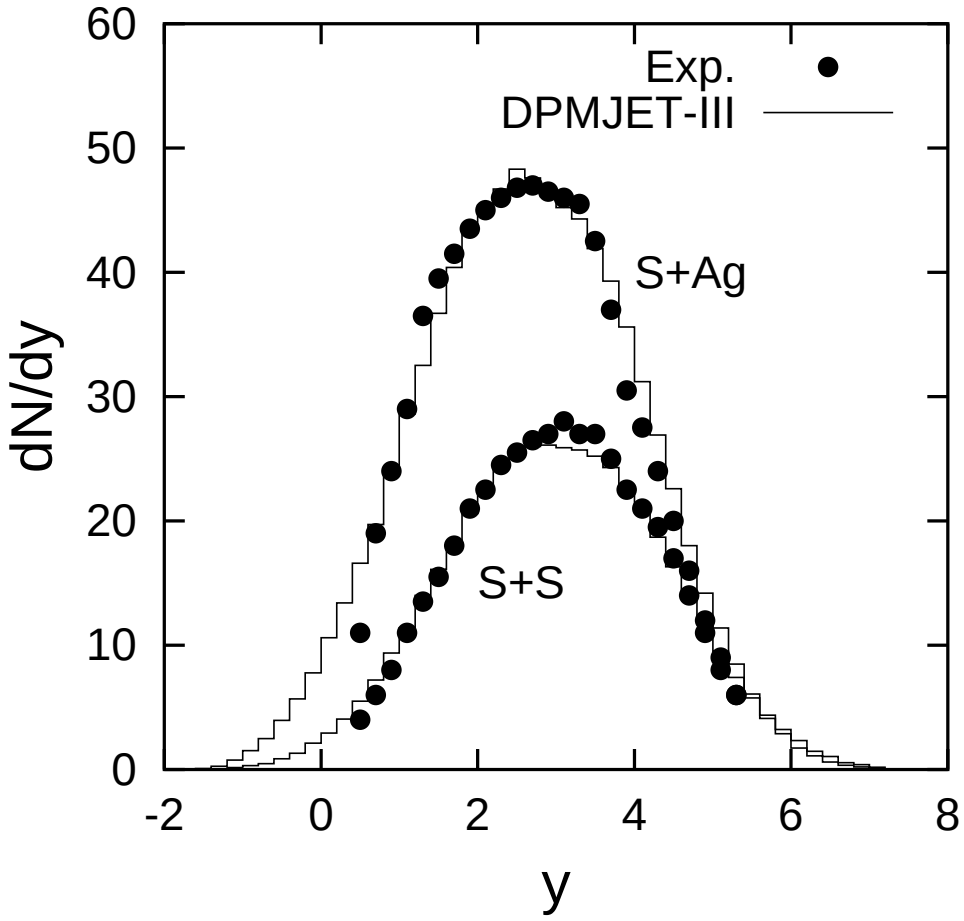

Rapidity distributions of negative hadrons in central nuclear collisions at 200 GeV/nucleon.

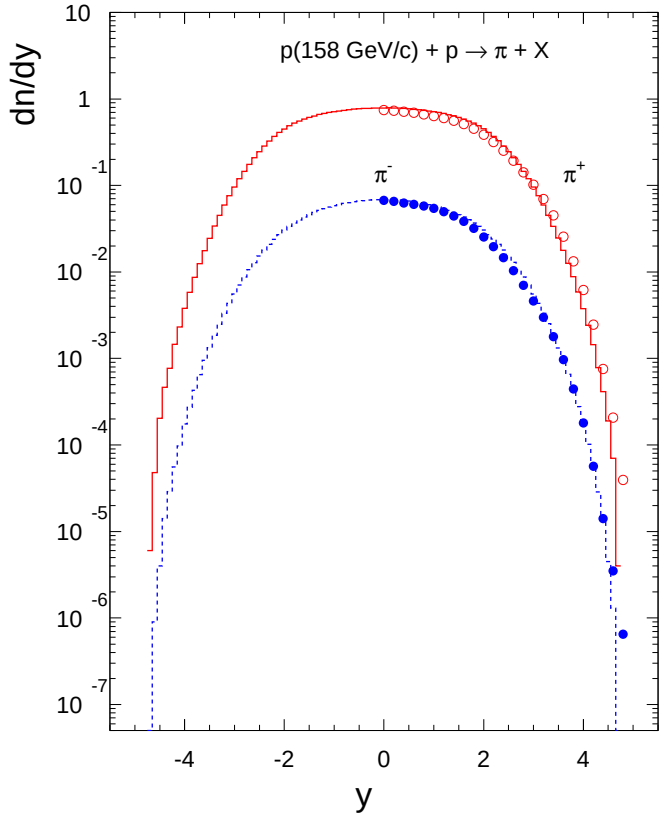

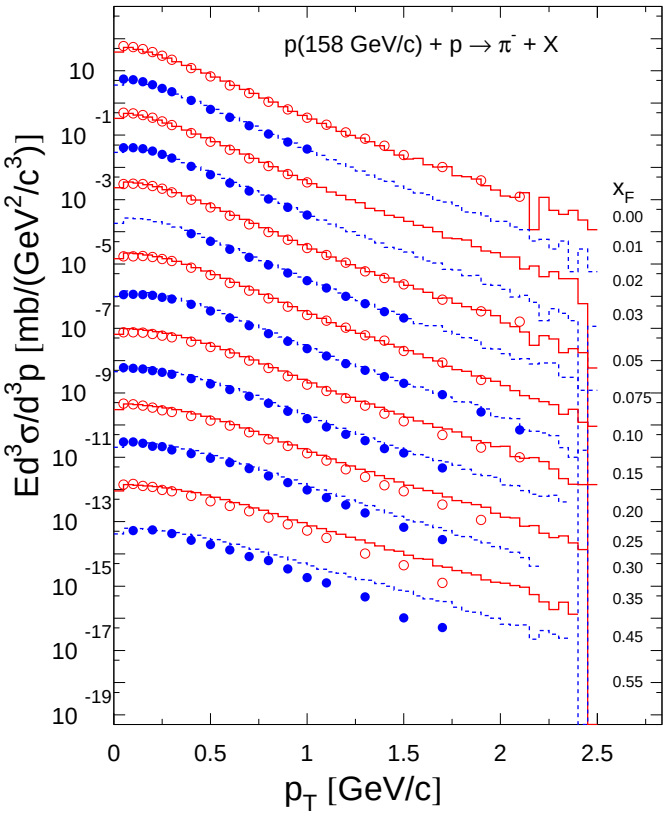

NA49 Collaboration: Comparison if pion production in 158 GeV p–p collisions with DPMJET–III results

(4) RHIC data and the DPM–models (DPMJET–III)

We first present some comparisons, where DPMJET-III is used in its pre–RHIC form:

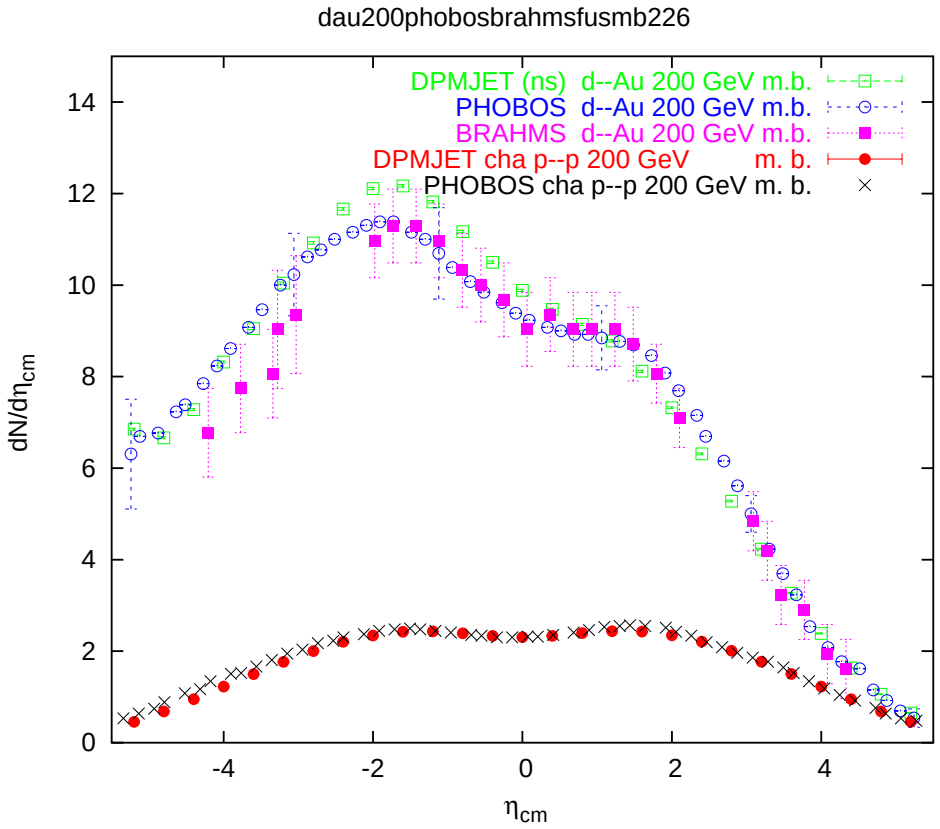

Pseudorapidity distribution of charged hadrons produced in minimum bias $\sqrt{s} = 200$ GeV d–Au and p–p collisions. The results of Dpmjet are compared to experimental data from the BRAHMS–Collaboration and the PHOBOS–Collaboration. At some pseudorapidity values the systematic PHOBOS–errors are given.

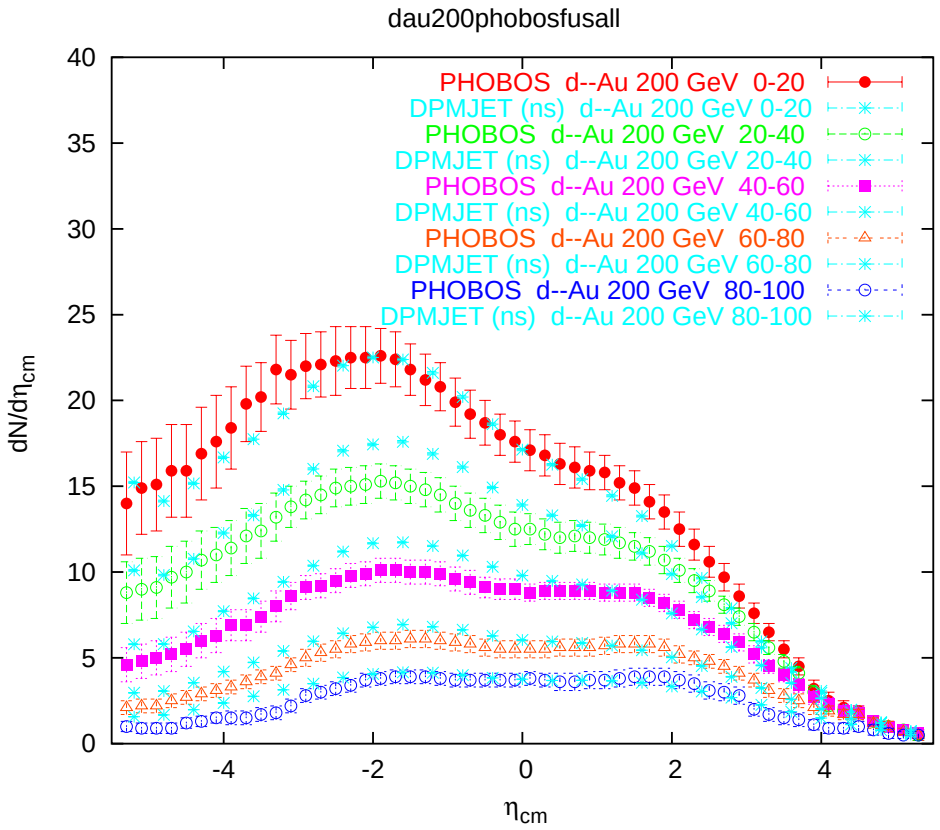

Pseudorapidity distribution of charged hadrons produced in non-single-diffractive (ns) $\sqrt{s} =$ 200 GeV d–Au collisions with different centralities. The results of Dpmjet are compared to preliminary data from the PHOBOS–Collaboration.

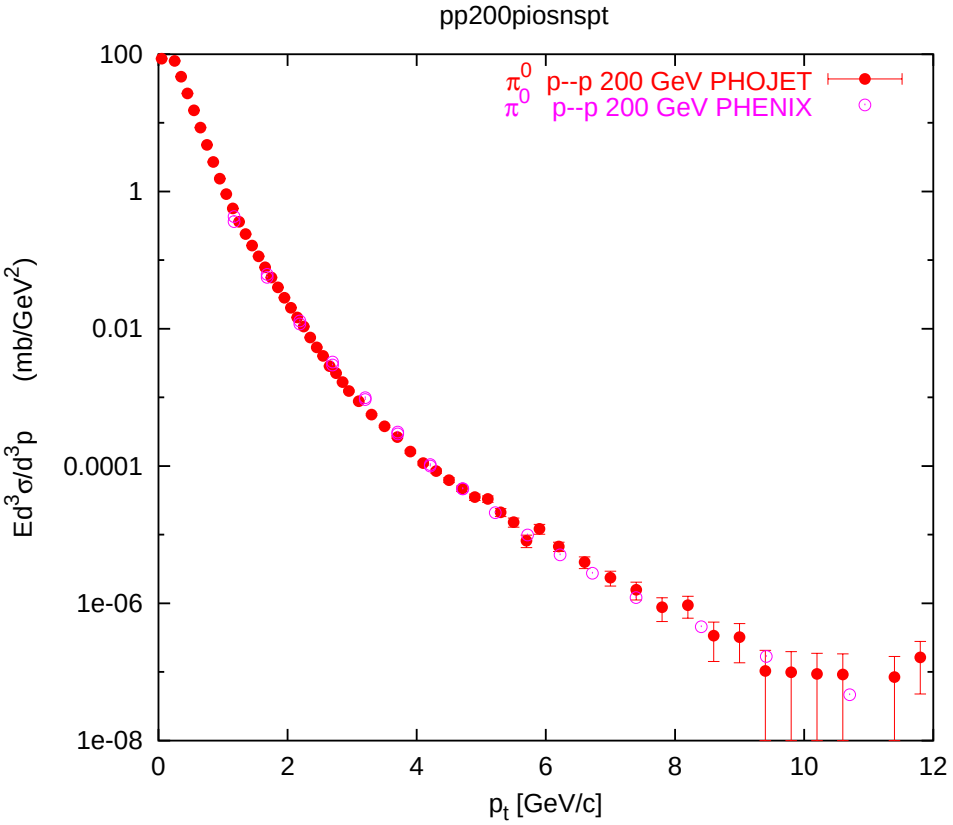

Transverse momentum distribution as measured in p–p collisions at $\sqrt{s} = 200$ GeV by the PHENIX collaboration at RHIC compared to the calculation by phojet

(4.2) For other comparisons DPM-JET needs some modifications to get agreement with the RHIC data.

The same modifications are needed in all models with hadron production via independent chain production

Percolation of hadronic strings in Dpmjet–III

Using the original Dpmjet–III with enhanced baryon stopping and a centrality of 0 to 5 % we compare to some multiplicities measured in Au–Au collisions at RHIC.

At $\sqrt{(s)} = 130$ GeV Dpmjet–III gives $N_{ch} = 6031$, BRAHMS finds $N_{ch} = 3860 \pm 300$.

Again at $\sqrt{(s)} = 130$ GeV Dpmjet–III gives a plateau $dN_{ch}/d\eta|_{\eta=0} = 968$, BRAHMS finds $dN_{ch}/d\eta|_{\eta=0} = 553 \pm 36$, PHOBOS finds $dN_{ch}/d\eta|_{\eta=0} = 613 \pm 24$ and PHENIX finds $dN_{ch}/d\eta|_{\eta=0} = 622 \pm 41$.

There is indeed a new mechanism needed to reduce N_{ch} and $dN_{ch}/d\eta|_{\eta=0}$ in situations with a produced very dense hadronic system.

Percolation of hadronic strings in Dpmjet–III

We consider only the percolation and fusion of soft chains (transverse momenta of both chain ends below a cut–off $p_{\perp}^{fusion} = 2$ GeV/c

The condition of percolation is, that the chains overlap in transverse space.

We calculate the transverse distance of the chains L and K R_{L-K} and allow fusion of the chains for $R_{L-K} \leq R^{fusion} = 0.75$ fm.

The chains in Dpmjet are fragmented using the Lund code

Only the fragmentation of color triplet–antitriplet chains is available in Jetset, however fusing two arbitrary chains could result in chains with other colors.

Therefore, we select only chains for fusion, which again result in triplet–antitriplet chains.

(i)A $q_1 - \bar{q}_2$ plus a $q_3 - \bar{q}_4$ chain become a $q_1 q_3 - \bar{q}_2 \bar{q}_4$ chain.

(ii)A $q_1 - q_2 q_3$ plus a $q_4 - \bar{q}_2$ chain become a $q_1 q_4 - q_3$ chain.

(iii)A $q_3 - q_1 q_2$ plus a $q_4 - \bar{q}_1$ plus a $\bar{q}_3 - q_5$ chain become a $q_4 - q_2 q_5$ chain.

(iv)A $q_4 - \bar{q}_1$ plus a $q_5 - \bar{q}_3$ plus a $\bar{q}_5 - q_1$ chain become a $q_4 - \bar{q}_3$ chain.

The expected results of these transformations are a decrease of the number of chains.

Even when the fused chains have a higher energy than the original chains, the result will be a decrease of the hadron multiplicity $N_{hadrons}$.

In reaction (i) we observe new diquark and anti–diquark chain ends. In the fragmentation of these chains we expect baryon–antibaryon production anywhere in the rapidity region of the collision.

Therefore, (i) helps to shift the antibaryon to baryon ratio of the model into the direction as observed in the RHIC experiments.

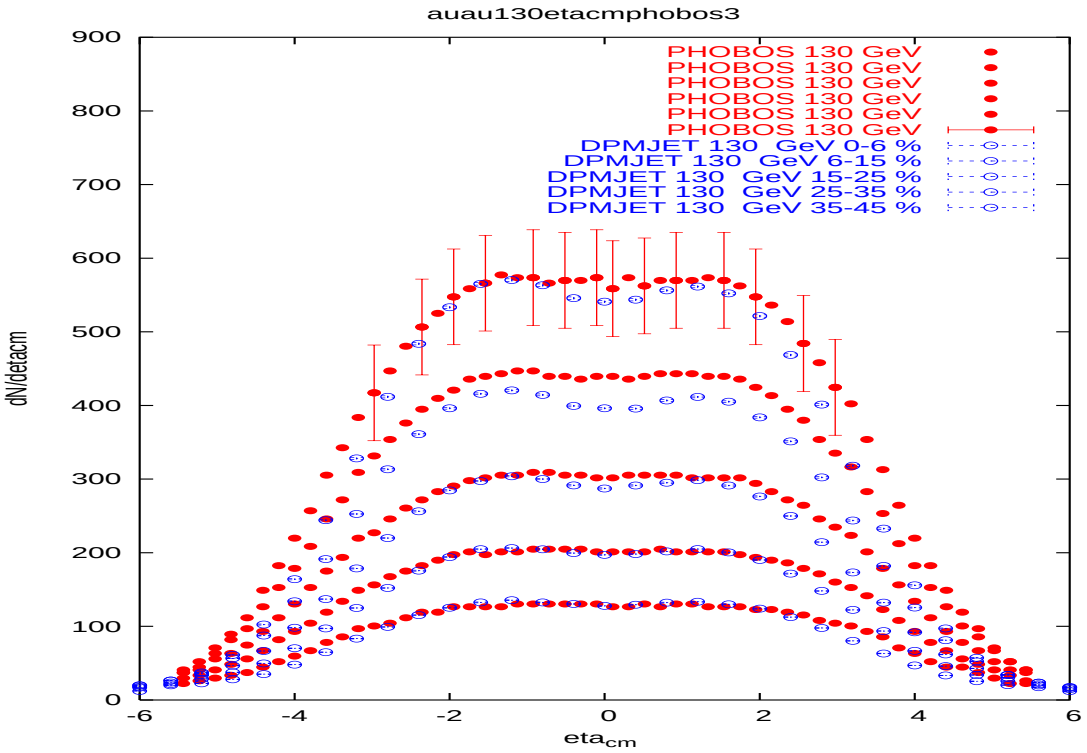

Pseudorapidity distributions of charged hadrons in Au–Au collisions at $\sqrt{(}s)$= 130 GeV for centralities 0–5 % up to 40–50 %. The points with rather small error bars are from the Dpmjet–III Monte Carlo with chain fusion as described in the text. The data points are from the PHOBOS Collaboration

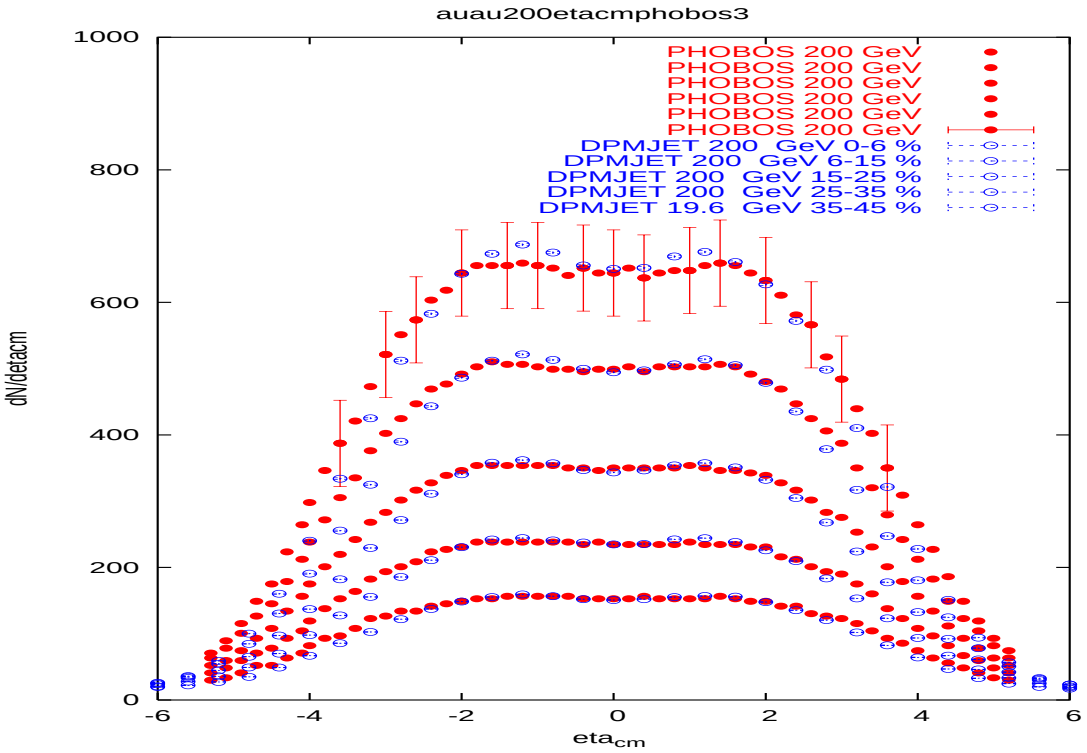

Pseudorapidity distributions of charged hadrons in Au–Au collisions at $\sqrt{(}s)$= 200 GeV for centralities 0–5 % up to 40–50 %. The points with rather small error bars are from the Dpmjet–III Monte Carlo with chain fusion as described in the text. The data points are from the PHOBOS Collaboration

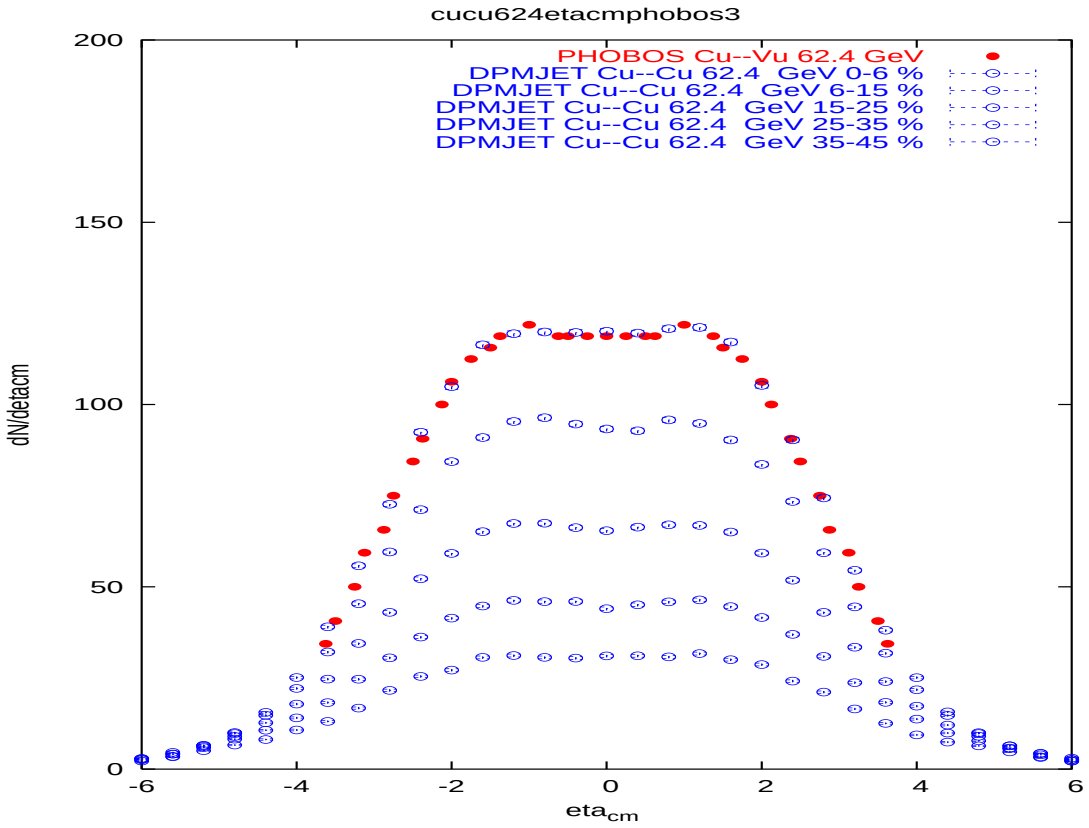

Pseudorapidity distributions of charged hadrons in Cu–Cu collisions at $\sqrt{(s)}$= 62.4 GeV for centralities 0–6 % up to 35–45 %. The points with rather small error bars are from the Dpmjet–III Monte Carlo with chain fusion as described in the text. The data points are from the PHOBOS Collaboration

Modified $p_\perp$ distributions in PYTHIA

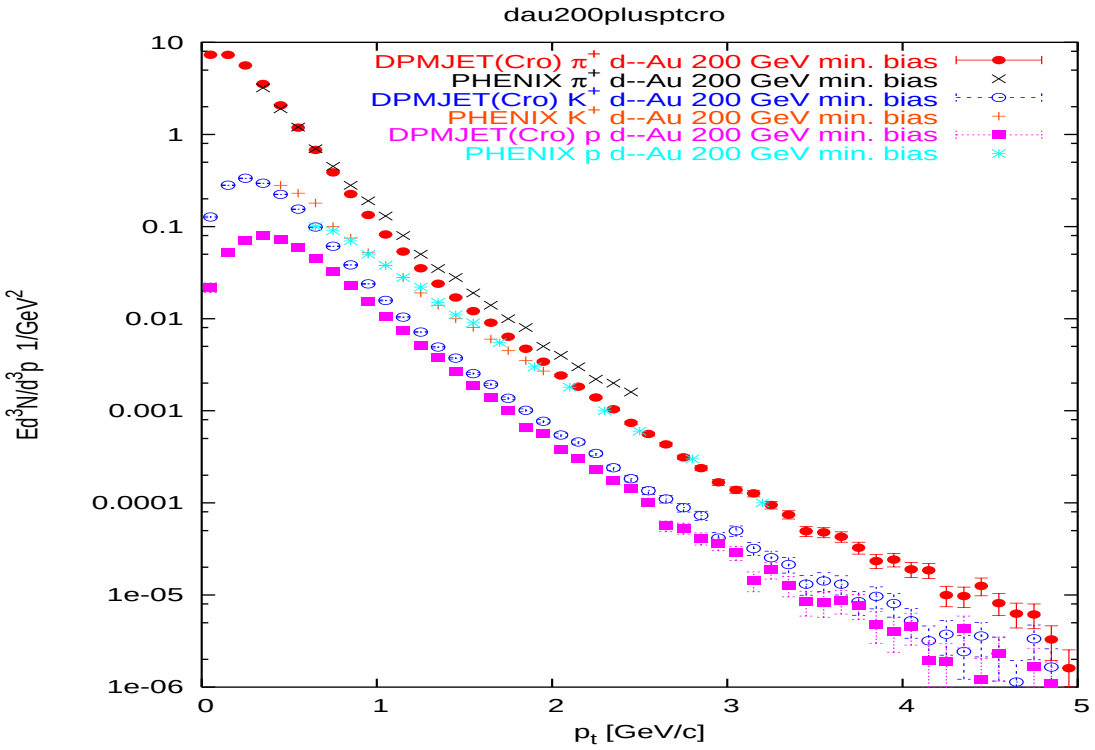

Transverse momentum distributions of positively charged hadrons in minimum bias d–Au collisions. Compared are the preliminary data from the PHENIX–Collaboration to the results of the original Dpmjet–III.

The Dpmjet–III model fails to describe the $p_\perp$ distributions of Kaons and protons.

This is the first time that we are able to compare the Dpmjet–III model to $p_\perp$ distributions of identified hadrons

The reason for this disagreement is the following:
DPMJET uses the PYTHIA code for the fragmentation of all chains (hard, QCD based chains as well as soft chains).
PYTHIA selects in the PYPTDI function the transverse momenta of (for instance) $q - \bar{q}$ pairs (to become hadrons finally) from independent Gaussians in the $p_{\perp x}$ and $p_{\perp y}$ components of $p_\perp$.

PYTHIA was extensively tested in processes with a significant hard component. For the fragmentation of the soft component this choice is not good.

It is known since very many years (given already in 1968 in a paper by Hagedorn and Ranft), that the transverse momentum distribution for hadrons with mass m in soft hadronic collisions is well described by an exponential in the transverse energy

$$\exp(-m_\perp/T), \qquad m_\perp = \sqrt{p_\perp^2 + m^2}. \tag{17}$$

We here chose a similar parametrization and replace the Gaussian in PYPTDI of PYTHIA by the distribution

$$\exp(-\sqrt{p_\perp^2 + m_x^2}/\sigma), \qquad m_x = 0.33 GeV/c. \tag{18}$$

After such a change all PYTHIA parameter which relate to the fragmentation have to be reoptimized.

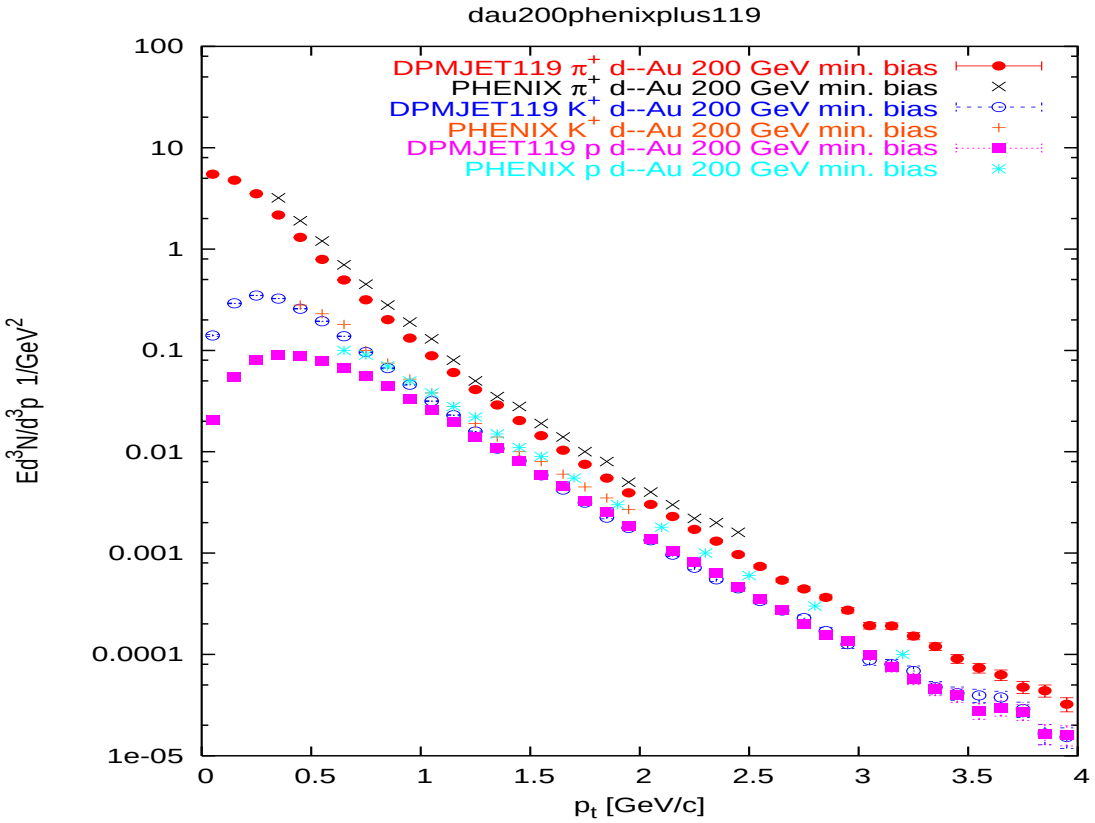

Transverse momentum distributions of positively charged hadrons in minimum bias d–Au collisions. Compared are the preliminary data from the PHENIX–Collaboration to the results of Dpmjet–III with modified transverse momentum distribution in hadronic soft chain decay as described in the paper.

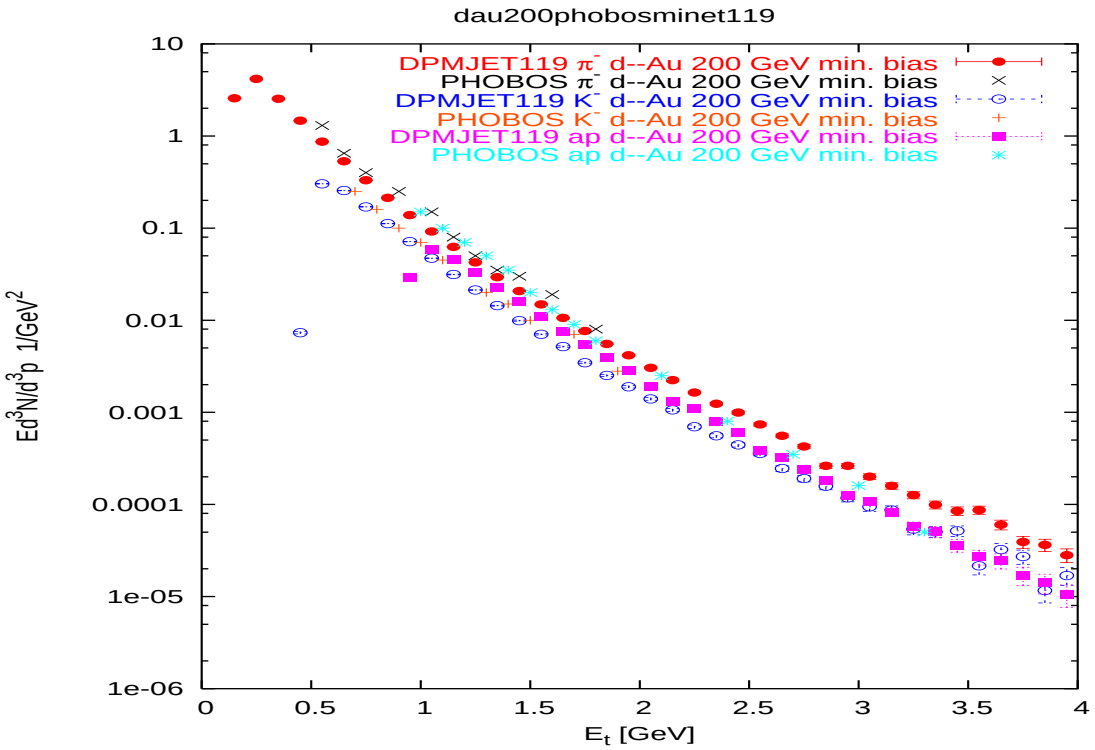

Transverse energy distributions of negatively charged hadrons in minimum bias d–Au collisions. Compared are the preliminary data from the PHOBOS–Collaboration to the results of Dpmjet–III with modified transverse momentum distribution in hadronic soft chain decay as described in the paper.

Collision scaling in h–A collisions

Several RHIC experiments (for instance PHENIX) find in d-Au collisions at large $p_\perp$ a nearly perfect collision scaling for π^0 production. Collision scaling means $R_{AA} \approx 1.0$.

The R_{AA} ratios are defined as follows:

$$R_{AA} = \frac{\frac{d^2}{dp_\perp d\eta} N^{A-A}}{N_{binary}^{A-A} \cdot \frac{d^2}{dp_\perp d\eta} N^{N-N}} \tag{19}$$

Here N_{binary}^{A-A} is the number of binary Glauber collisions in the nucleus–nucleus collision A–A.

Dpmjet–III in its original form gave for π^0 production in d+Au collisions strong deviations from collision scaling ($R_{AA} \approx 0.5$ at large $p_\perp$).

The reason for this was in the iteration procedure to sample the multiple collisions in Dpmjet:

some soft and hard collisions were rejected by this iteration procedure.

Using a reordered iteration procedure it was possible to obtain a nearly perfect collision scaling, see the next Fig.

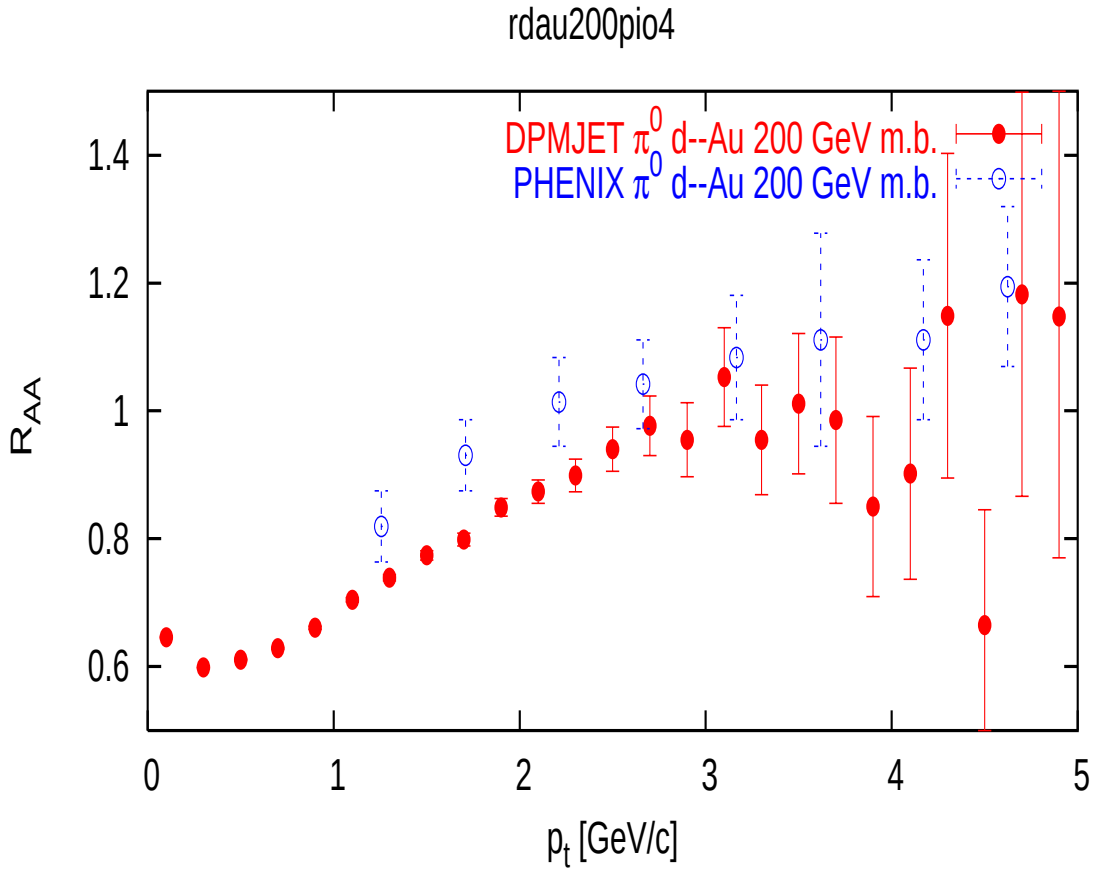

R_{AA} ratio of π^0–mesons produced in $\sqrt{s} = 200$ GeV d–Au collisions. The results of the modified Dpmjet are compared to experimental data from the PHENIX–Collaboration.

Remark: New physics in central collisions at RHIC:

These are features, which can not be explained in independent chain production models.

PHENIX, RHIC: Large $p_\perp$ supression in central collisions

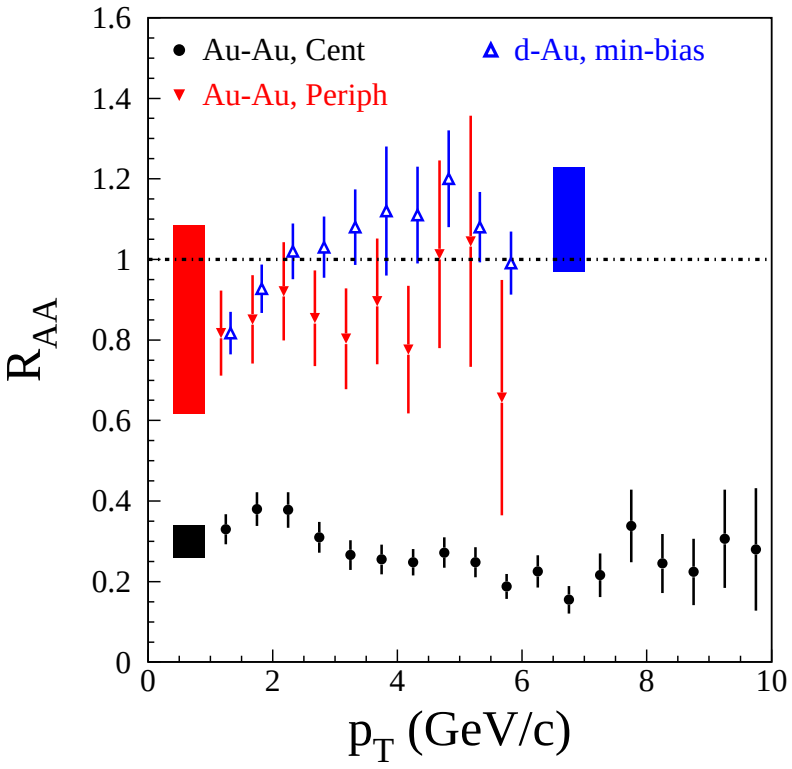

$$R_{AA} = \frac{\frac{d^2}{dp_\perp d\eta} N^{A-A}}{N^{A-A}_{binary} \cdot \frac{d^2}{dp_\perp d\eta} N^{N-N}} \qquad (20)$$

STAR, RHIC: Supression of back–to–back jet

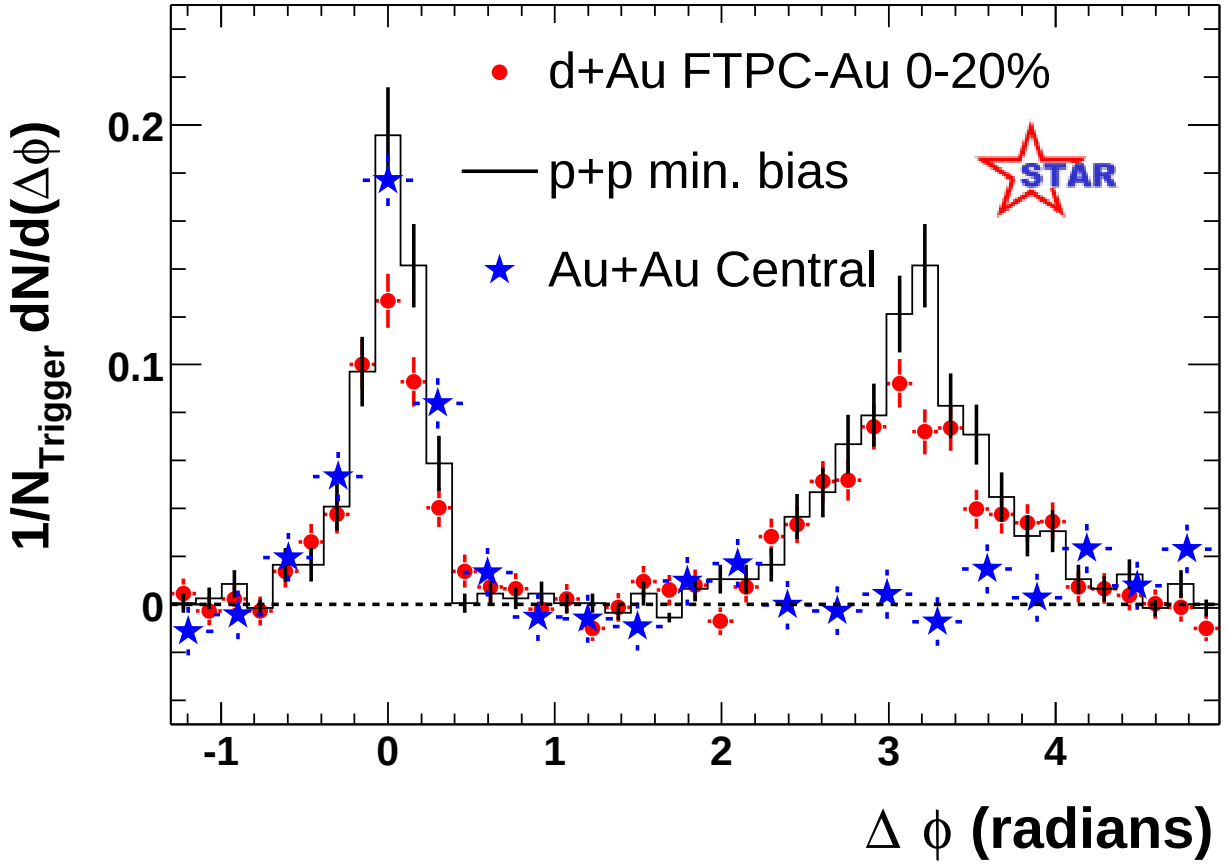

Further RHIC related improvements (not treated here) in DPM-JET include:

Anomalous baryon stopping: New diagrams lead to more baryons in central region.

Modified diquark fragmentation: Find missing diagram in di-quark fragmentation, to get Antihyperon to Hyperon ratios into agreement with experiment.

(5) Model comparisons

We start with one example to demonsrate the big dfferences in a case, where no experimental data are available

We present x_{lab} distributions of produced particles in Fe–N collisions. According to the SIBYLL–1.7 , QGSJET and Dpmjet–III models.

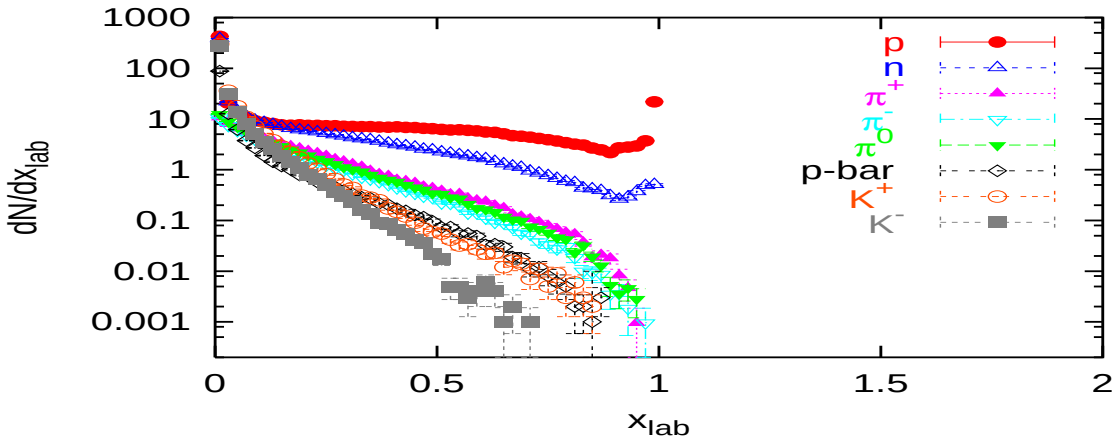

SIBYLL-1.7

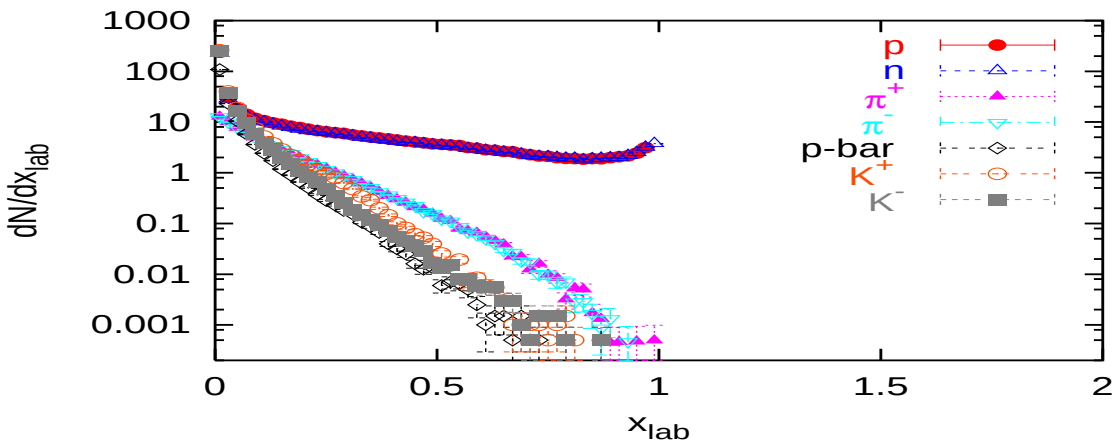

QGSJET model

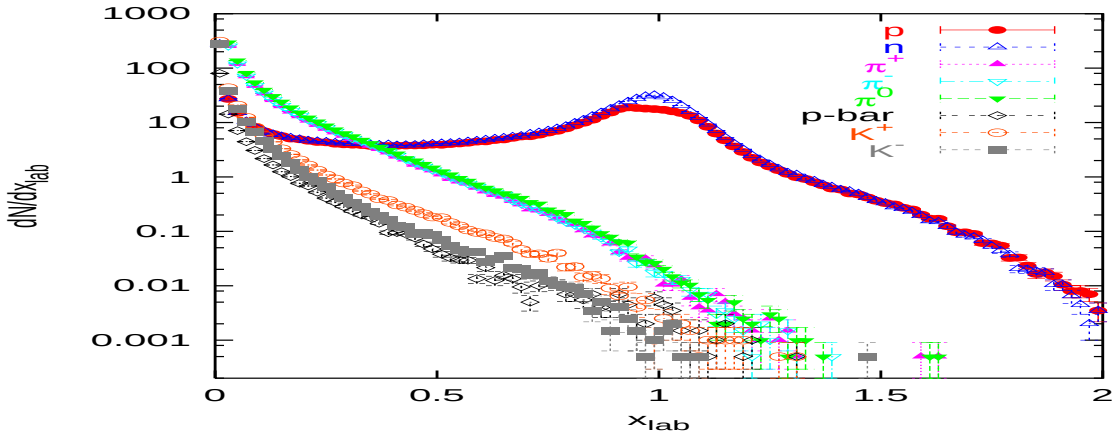

DPMJET-III

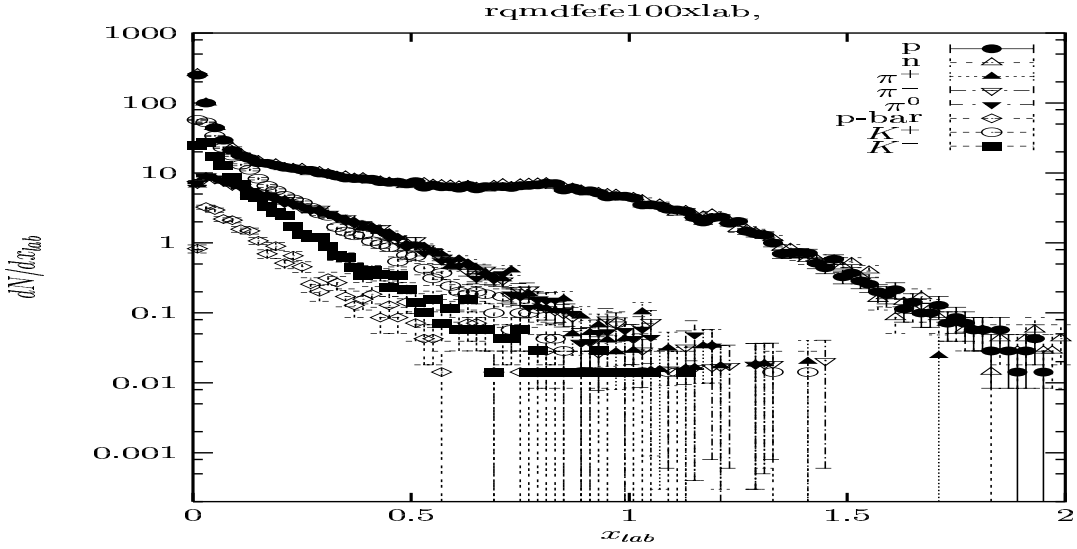
rqmdfefe100xlab,
1000
100
10
1
0.1
0.01
0.001
0
0.5
1
1.5
2
x_{lab}
dN/dx_{lab}
p
n
π+
π−
π0
p-bar
K+
K−

1

RQMD model

We observe significant differences between the four models. In SIBYLL–1.7, the secondary p and n distributions differ, in the three other models they are nearly identical.

In Dpmjet–III, the Fermi momentum of the nucleons in both colliding nuclei is included, therefore the x_{lab} distributions extend well above $x_{lab} = 1$,

in SIBYLL–1.7 and QGSJET the Fermi momentum is not included and the x_{lab} distributions stop at $x_{lab} = 1$.

In the RQMD model which also includes Fermi momenta we find x_{lab} distributions quite similar to the ones from Dpmjet–III.

It is clear from this comparison, data are urgently needed to guide the models. Unfortunately, forward hadron production so far has not been measured, also not at the RHIC collider.

(5.2) D.Heck, Karlsruhe, Comparison of models in the CORSIKA Cosmic Ray cascade code

Dieter Heck, Forschungszentrum Karlsruhe,Institut fuer Kernphysik

VIHKOS CORSIKA School 2005, Lauterbad, Germany, May 31 – June 5, 2005

The Influence of hadronic interaction models on simulated air showers: A phenomenologic comparison.

Dieter Heck, private communication: This are about 75 percent of the comparisons I will present.

High energy models in CORSIKA $E_{lab} \geq$ 80 GeV

DPMJET 2.55

NEXUS 2/3

QGSJET 01/II/III

SIBYLL 2.1

Low energy models in CORSIKA $E_{lab} \leq$ 80 GeV

FLUKA 2003 (only hadron production model)

GHEISHA 2002 (no longer recommended)

UrQMD 1.3

References

DPMJET 2.55 J.Ranft,Phys.Rev.D51 (1995) 64

NEXUS 2/3 J.Drescher et al., Phys.Rep.350 (2001) 93

QGSJET 01/II/III S.Ostapchenko, Nucl.Phys.B(Proc.Suppl.)2005

SIBYLL 2.1 R.Engel et al.,Proc.26th ICRC 1(1999)415

FLUKA 2003 A.Fasso et al.,Proc.Monte Carlo 2000 (2001)955

GHEISHA 2002 H.Fesefeld, PITHA–85/02 Aachen (1985)

UrQMD 1.3 S.A.Bass et al.,Prog.Part.Nucl.Phys.41 (1998)225

$\pi^{\pm}$ average multiplicities in p–p collisions

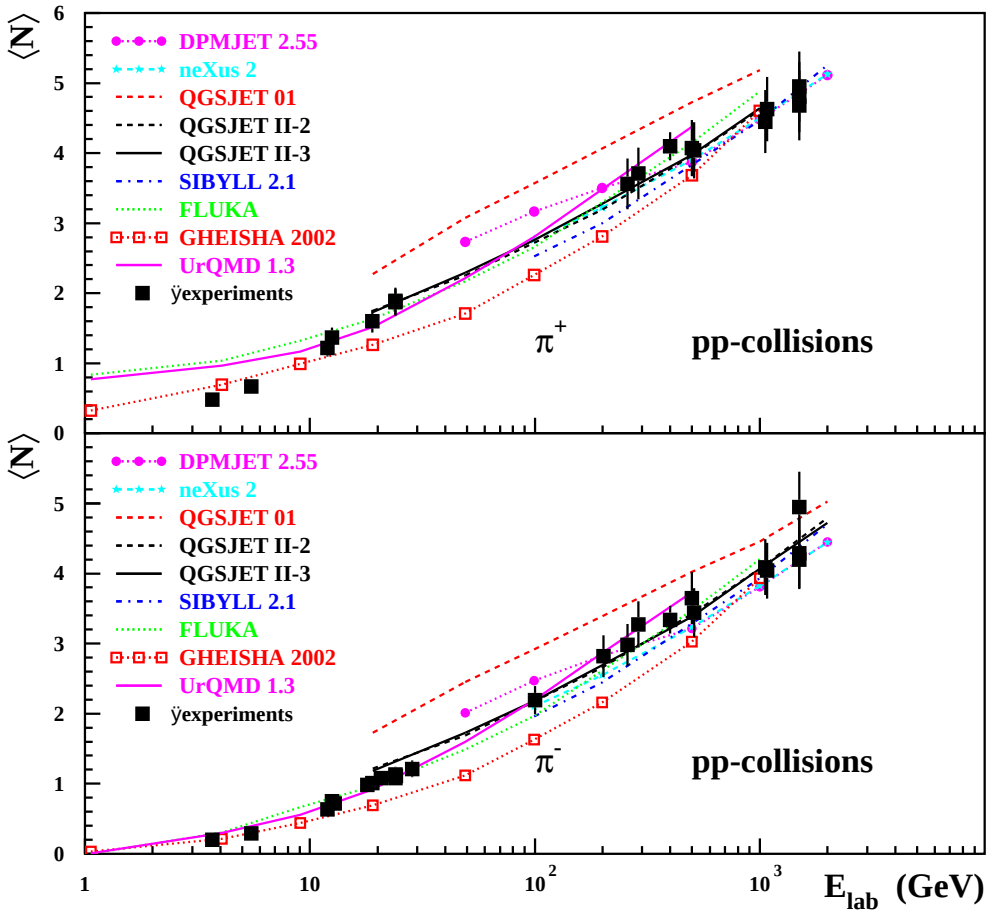

Charged particle multiplicity distribution in p–$\bar{p}$ collisions at E_{CM} = 900 GeV.

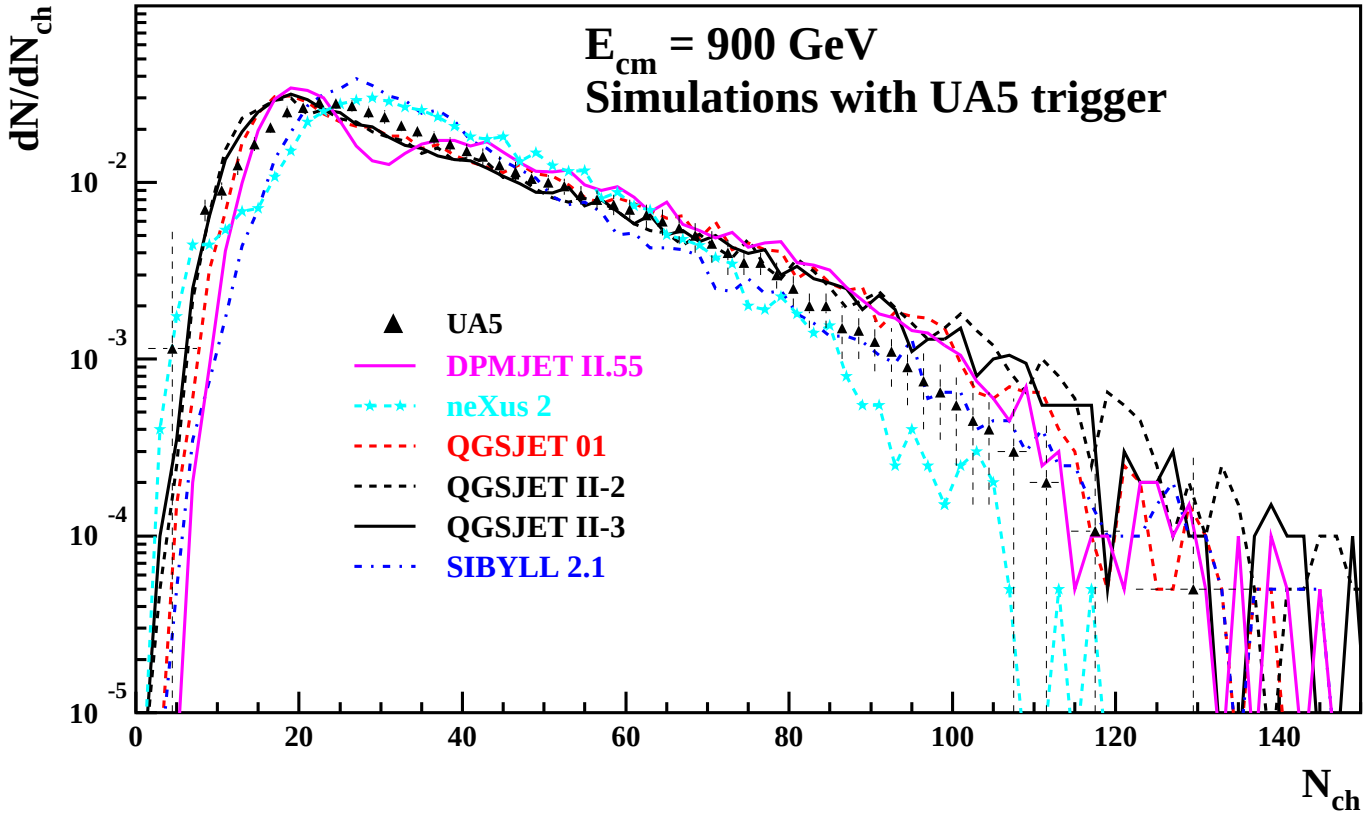

Charged particle multiplicity distribution in p–$\bar{p}$ collisions at E_{lab} = 10^{19} eV.

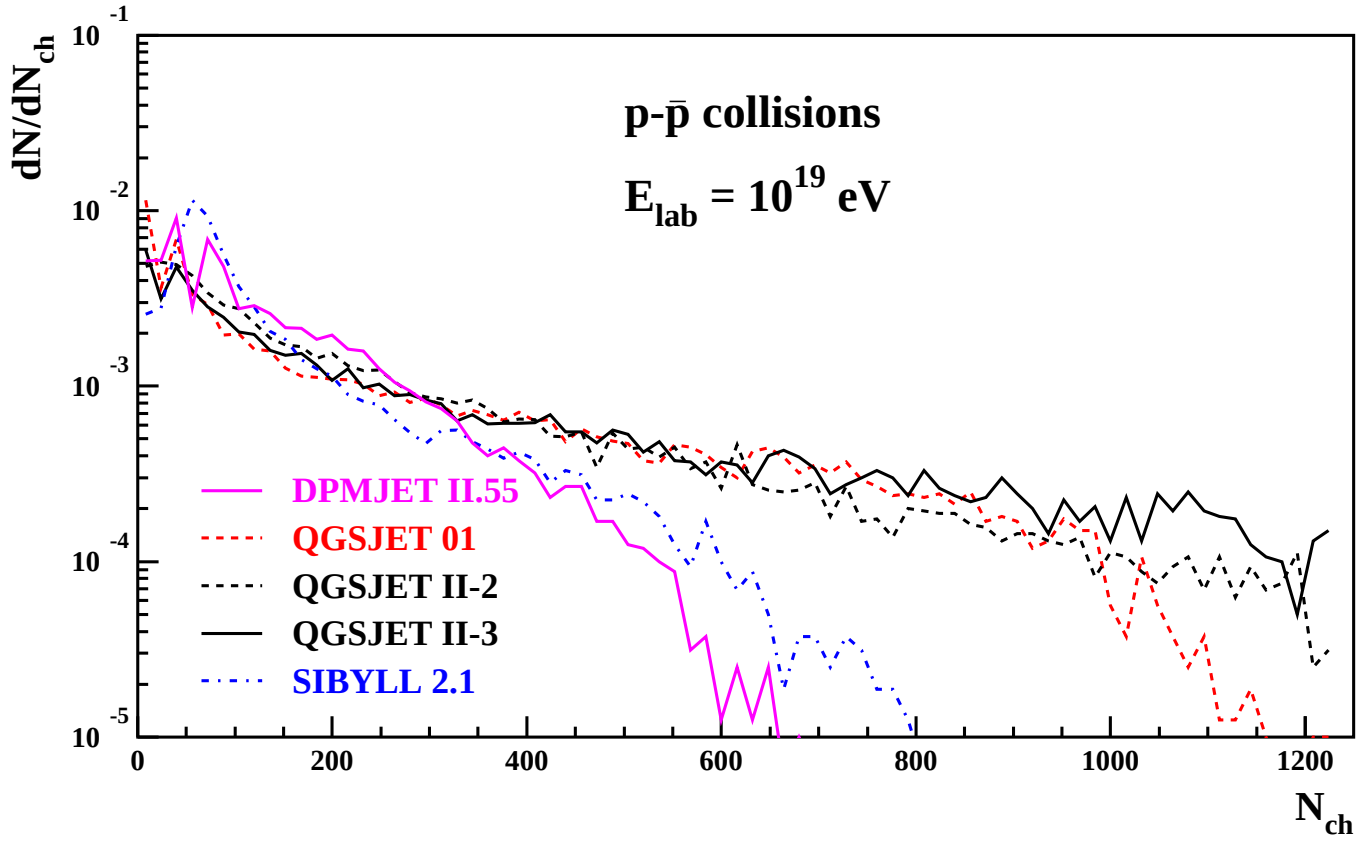

Charged particle average multiplicity in p–$\bar{p}$ collisions.

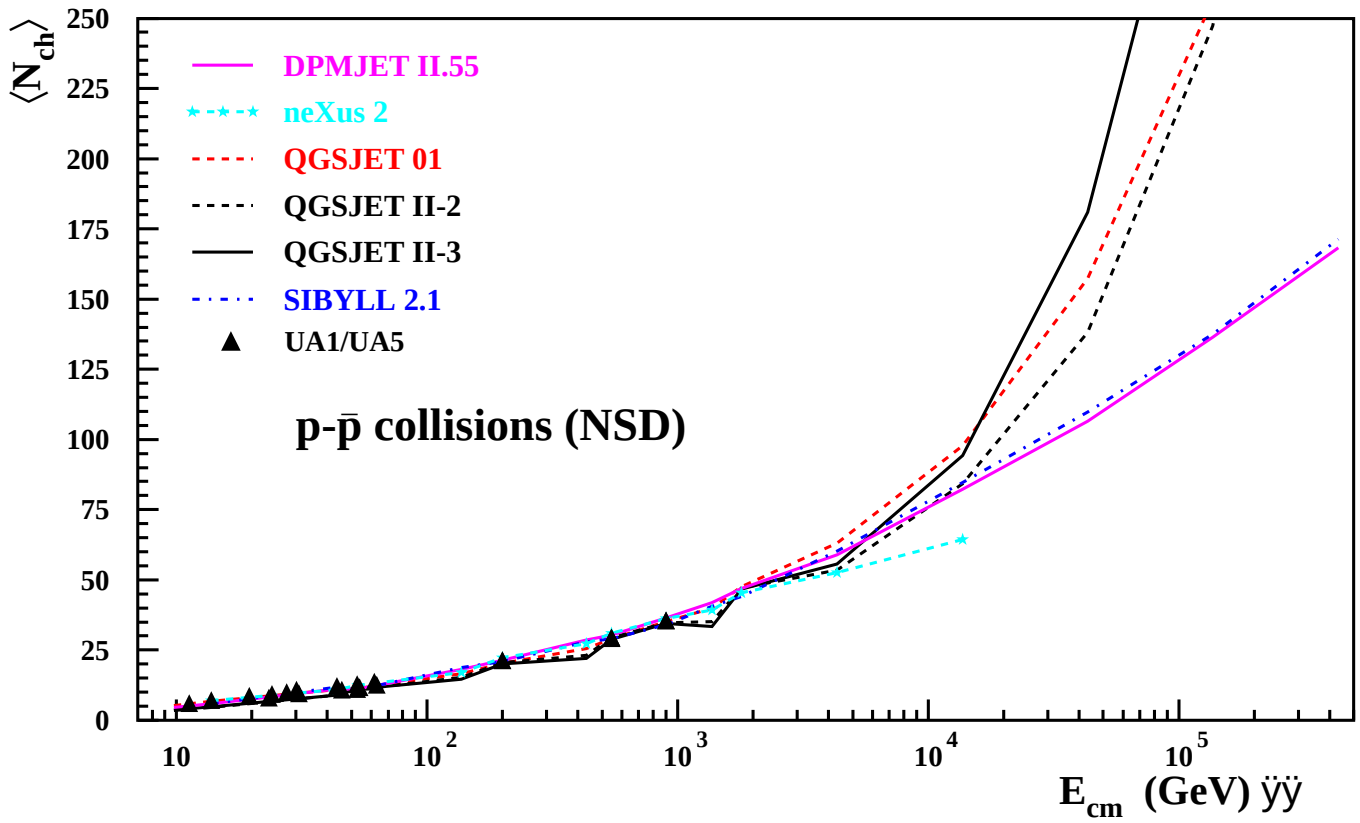

Pseudo–rapidity distribution of charged particles in p–$\bar{p}$ collisions at $E_{CM} = 900$ GeV.

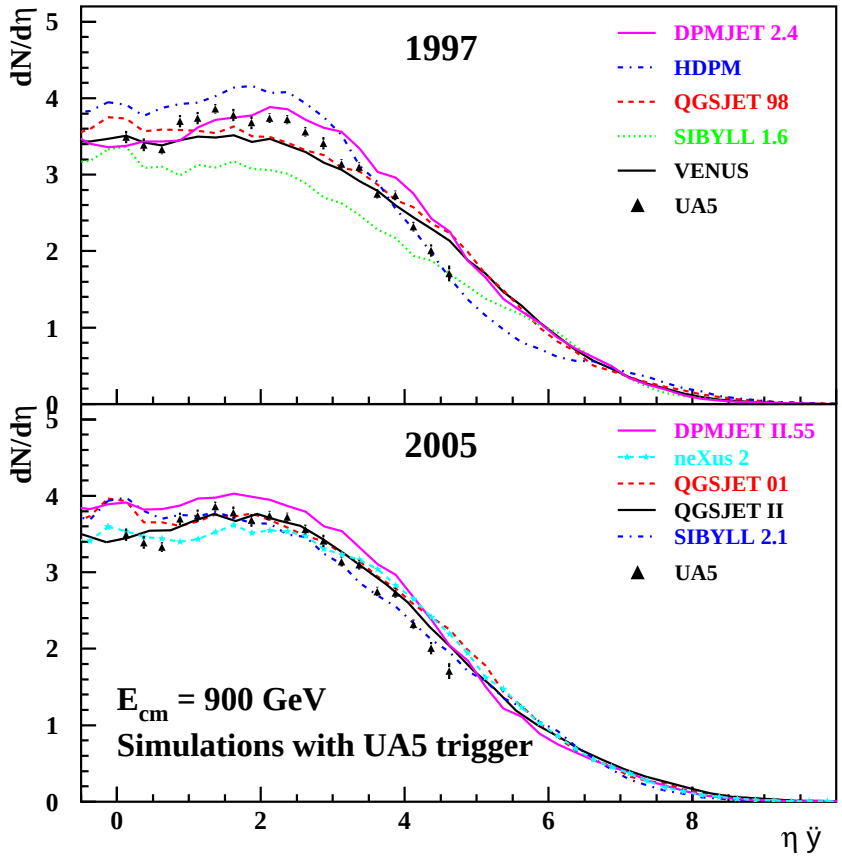

Pseudo–rapidity distribution of charged particles in p–$\bar{p}$ collisions at $E_{CM} = 630$ GeV.

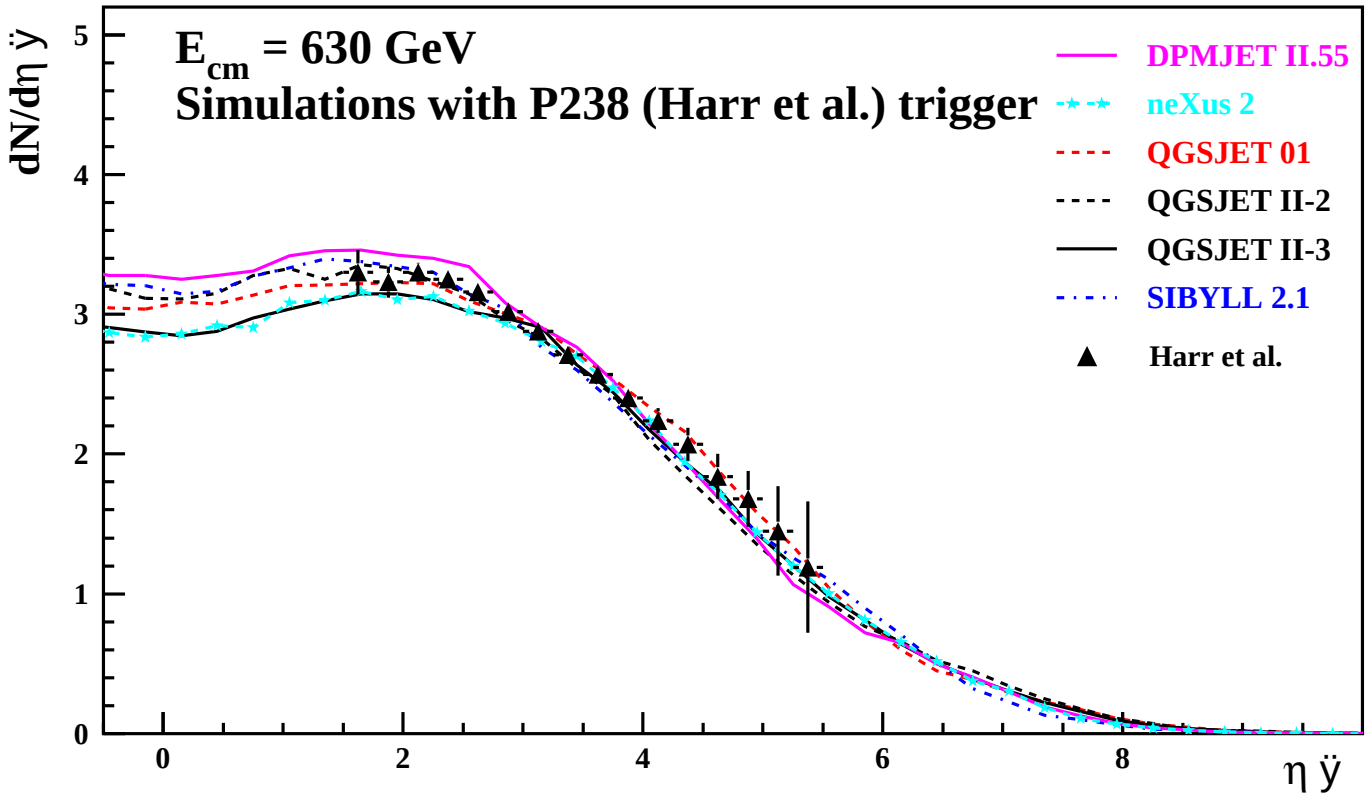

Pseudo–rapidity distribution of charged particles in p–$\bar{p}$ collisions at $E_{lab} = 10^{19}$ eV.

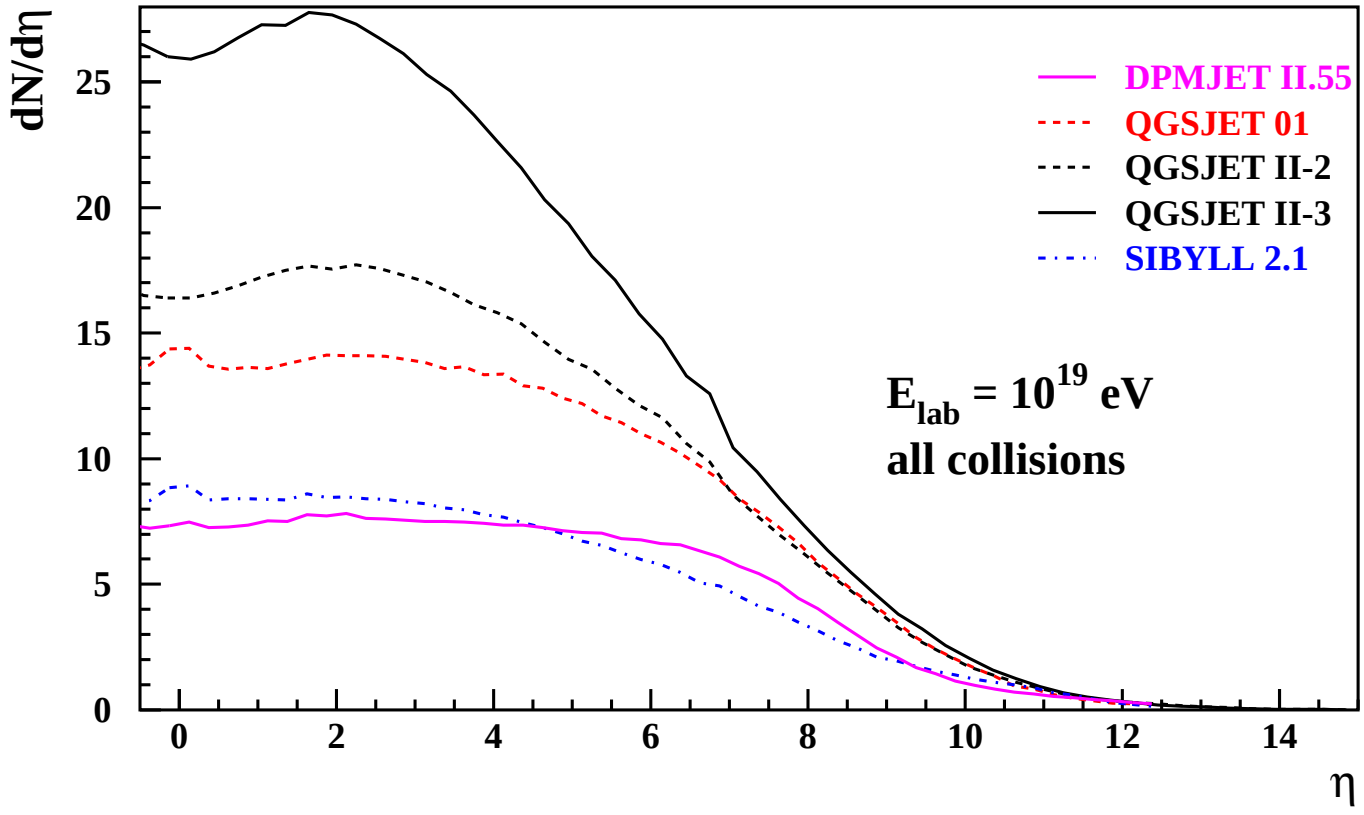

x_{lab} distribution of most–energetic baryons in p–$\bar{p}$ collisions at $E_{lab} = 10^{15}$ eV.

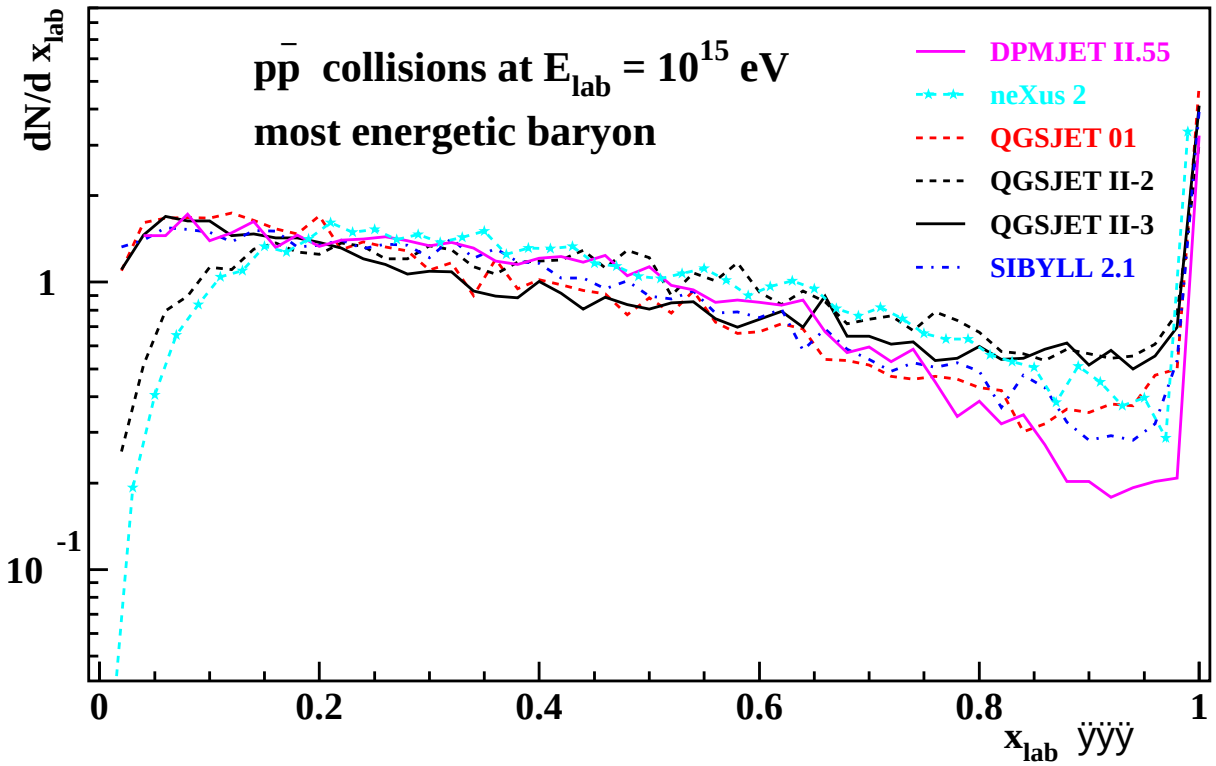

x_{lab} distributions (multiplied with x_{lab}) of $\pi^{\pm}$ mesons in p–^{9}Be collisions at $p_{lab} = 24$ GeV.

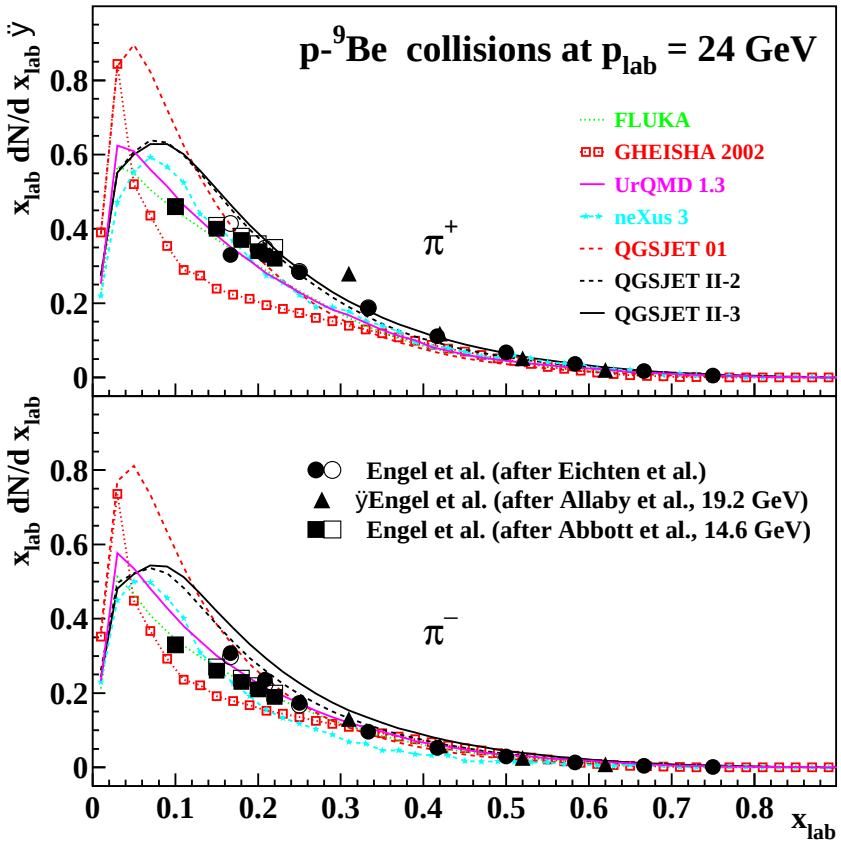

x_{lab} distributions (multiplied with x_{lab}) of π^- mesons in p–^9C collisions at p_{lab} = 4.2 and 10 GeV.

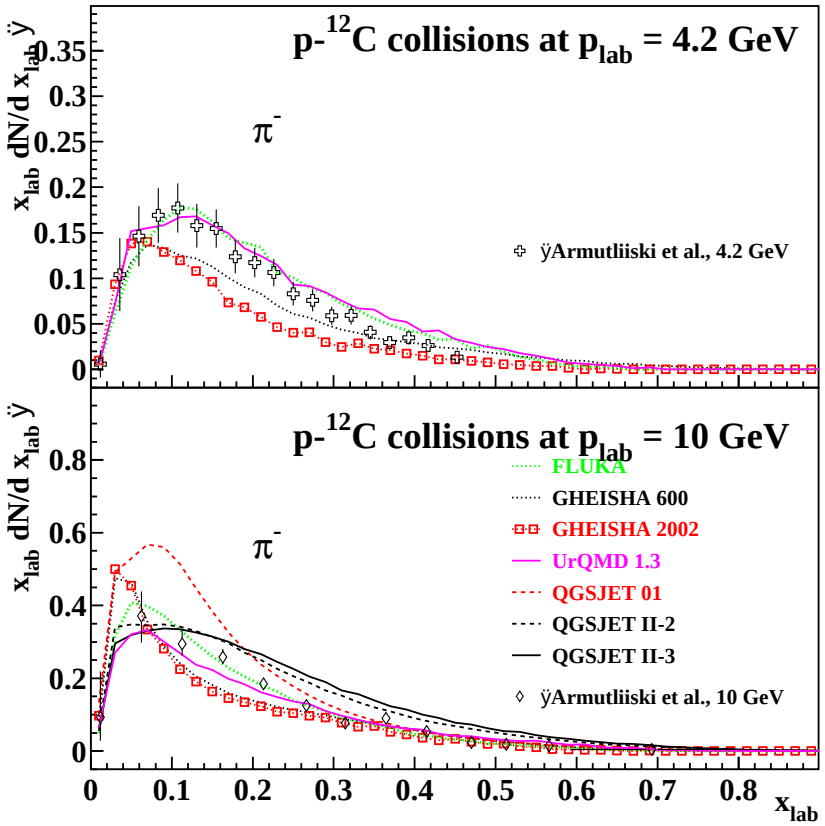

Charged particle multiplicity distribution p–^{14}N collisions at E_{lab} = 10^{19} eV.

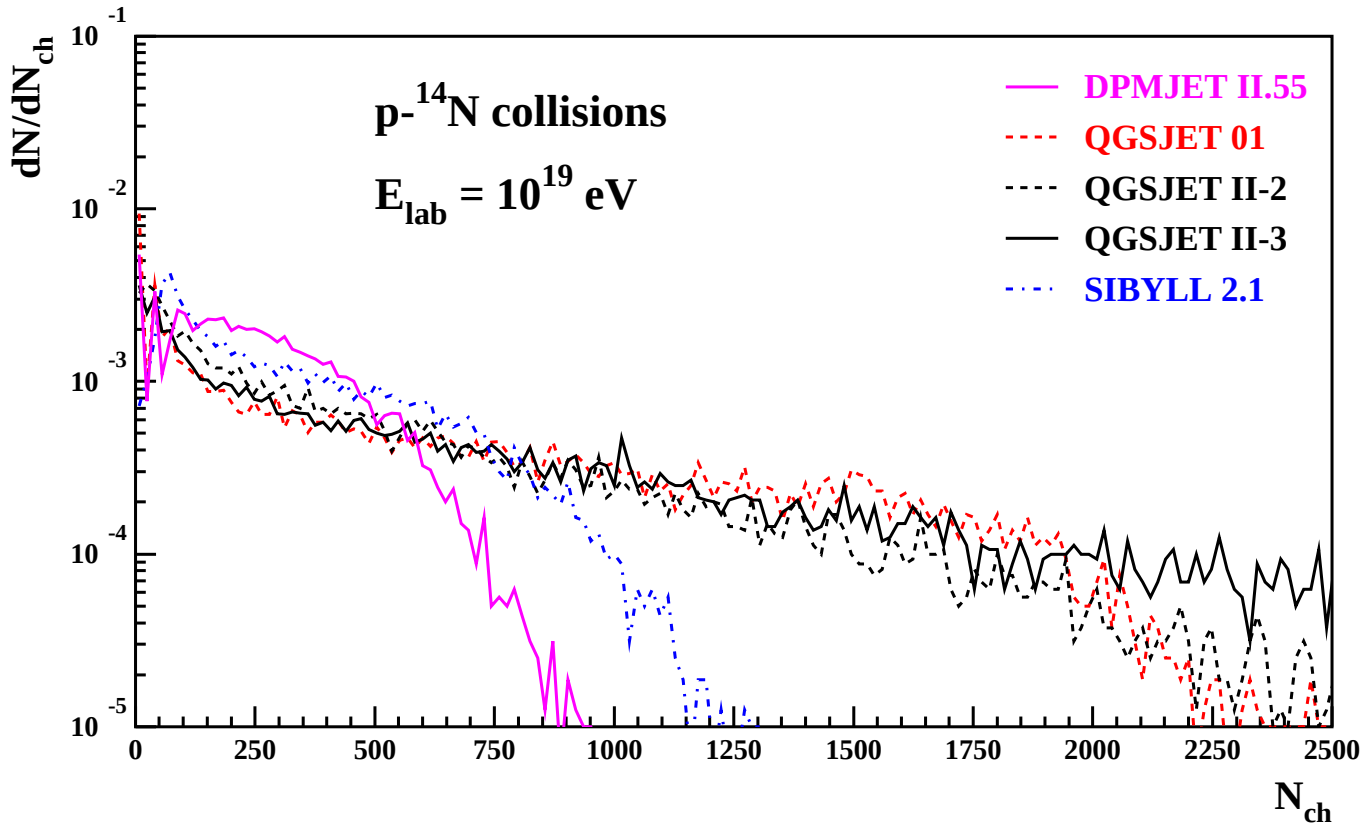

Charged particle multiplicity distribution in π^+–^{14}N collisions at $E_{lab} = 10^{15}$ eV.

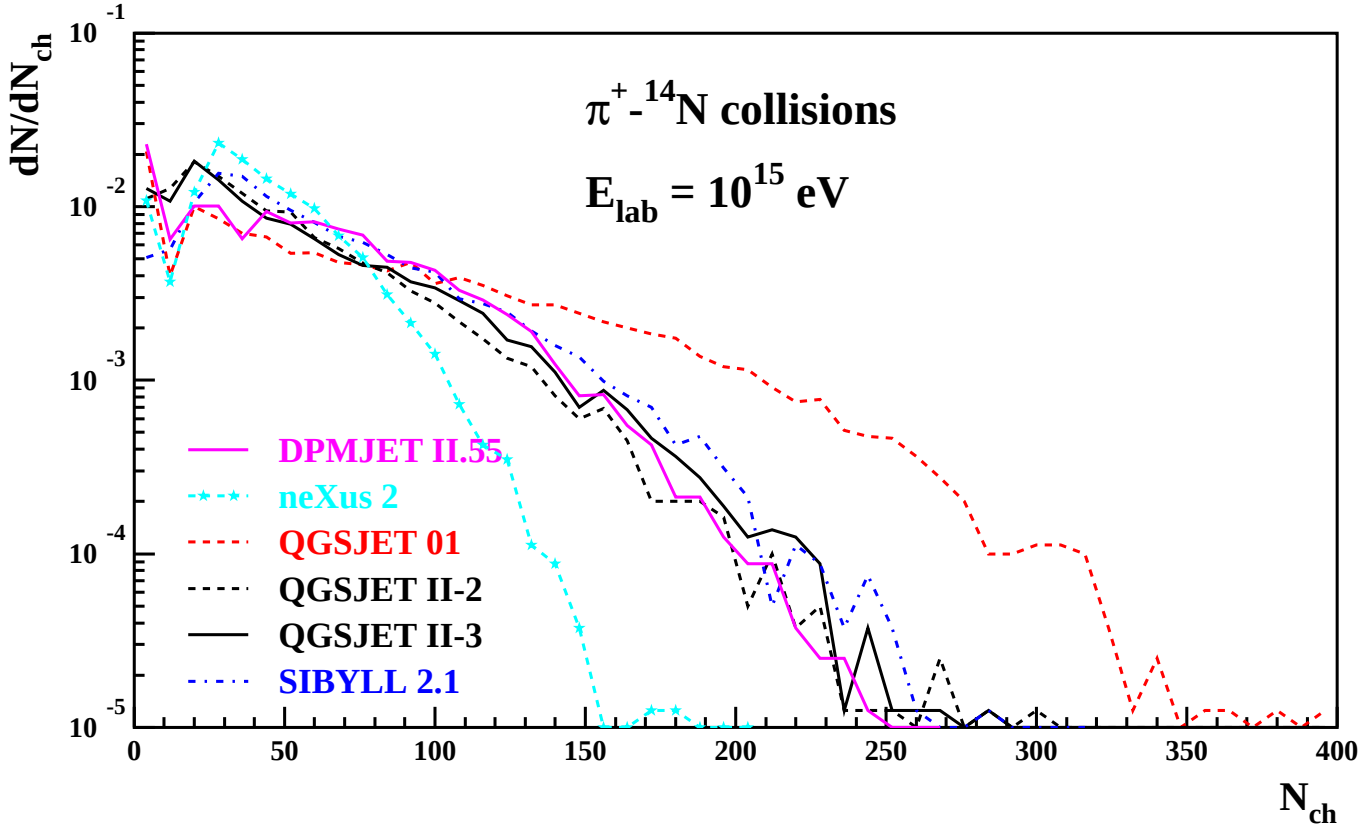

Charged particle average multiplicity distribution in π^+–^{14}N collisions at $E_{lab} = 10^{19}$ eV.

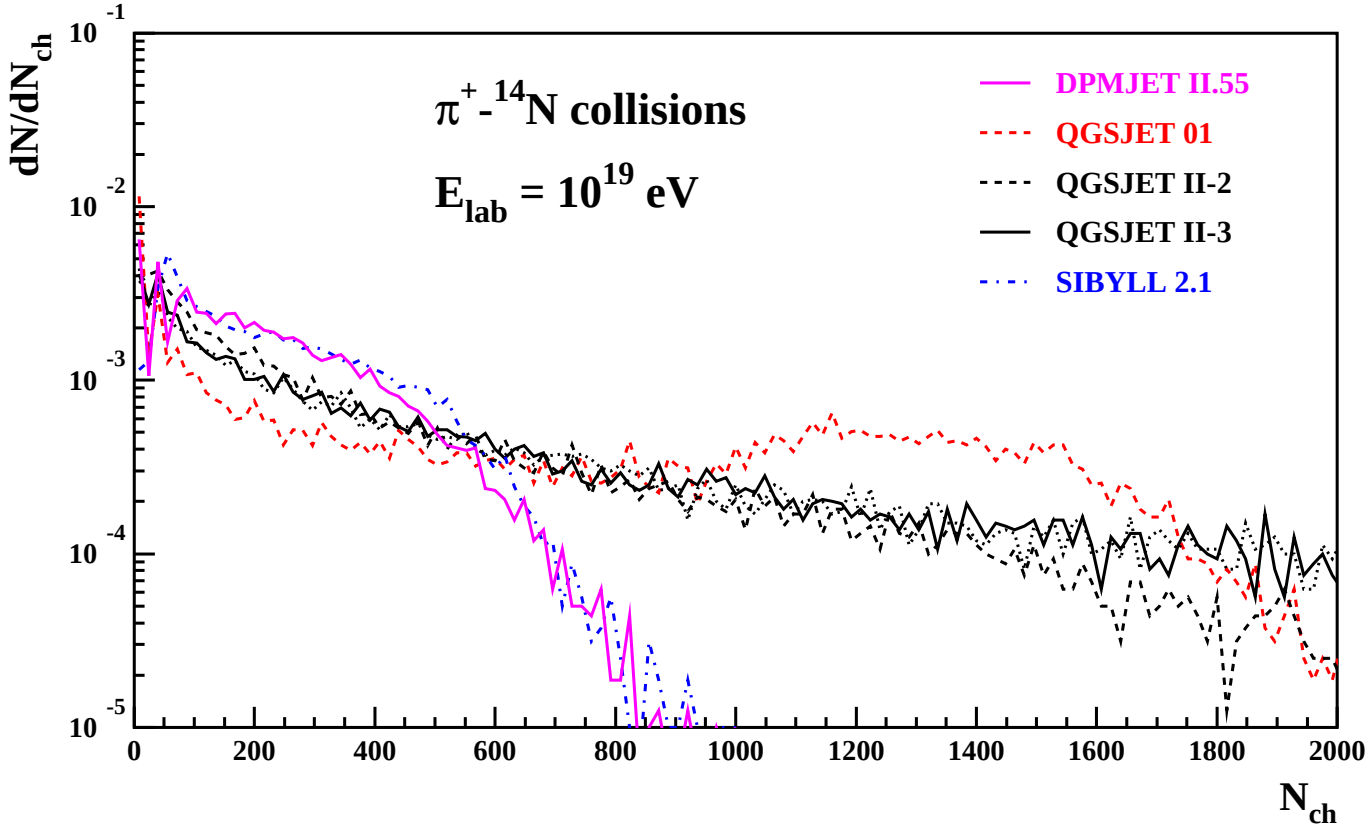

Inelastic proton–Air cross–sections.

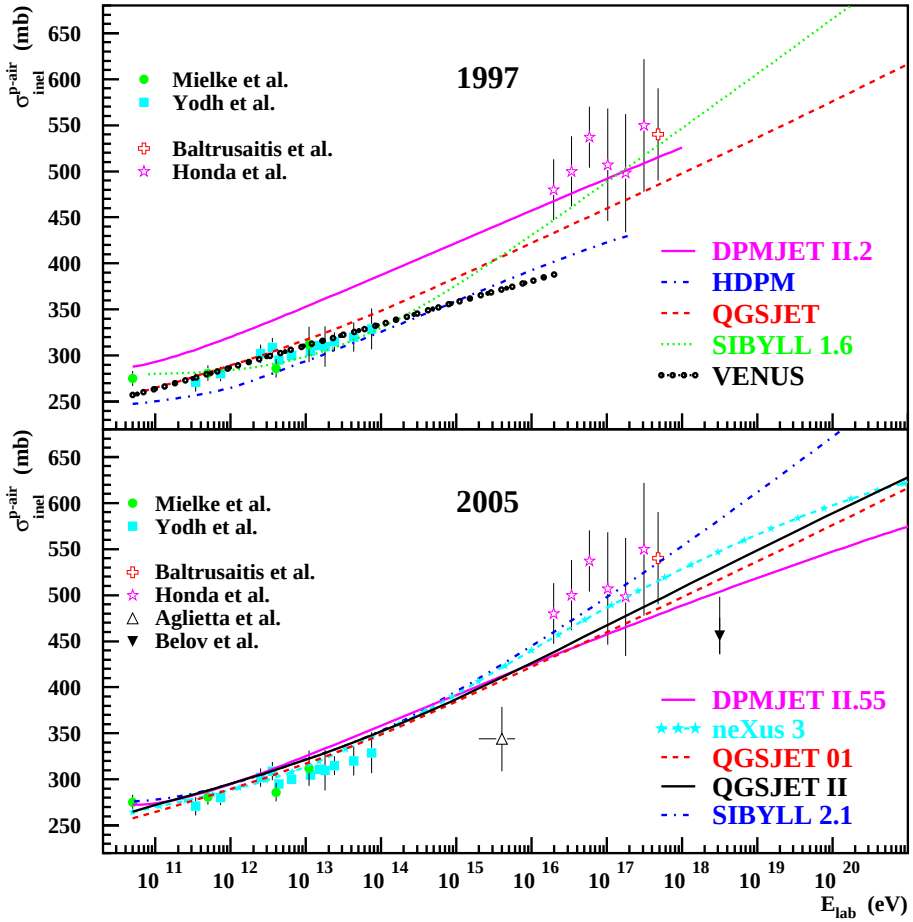

Electron number distributions for proton induced vertical showers of 10^{14} to 10^{17} eV.

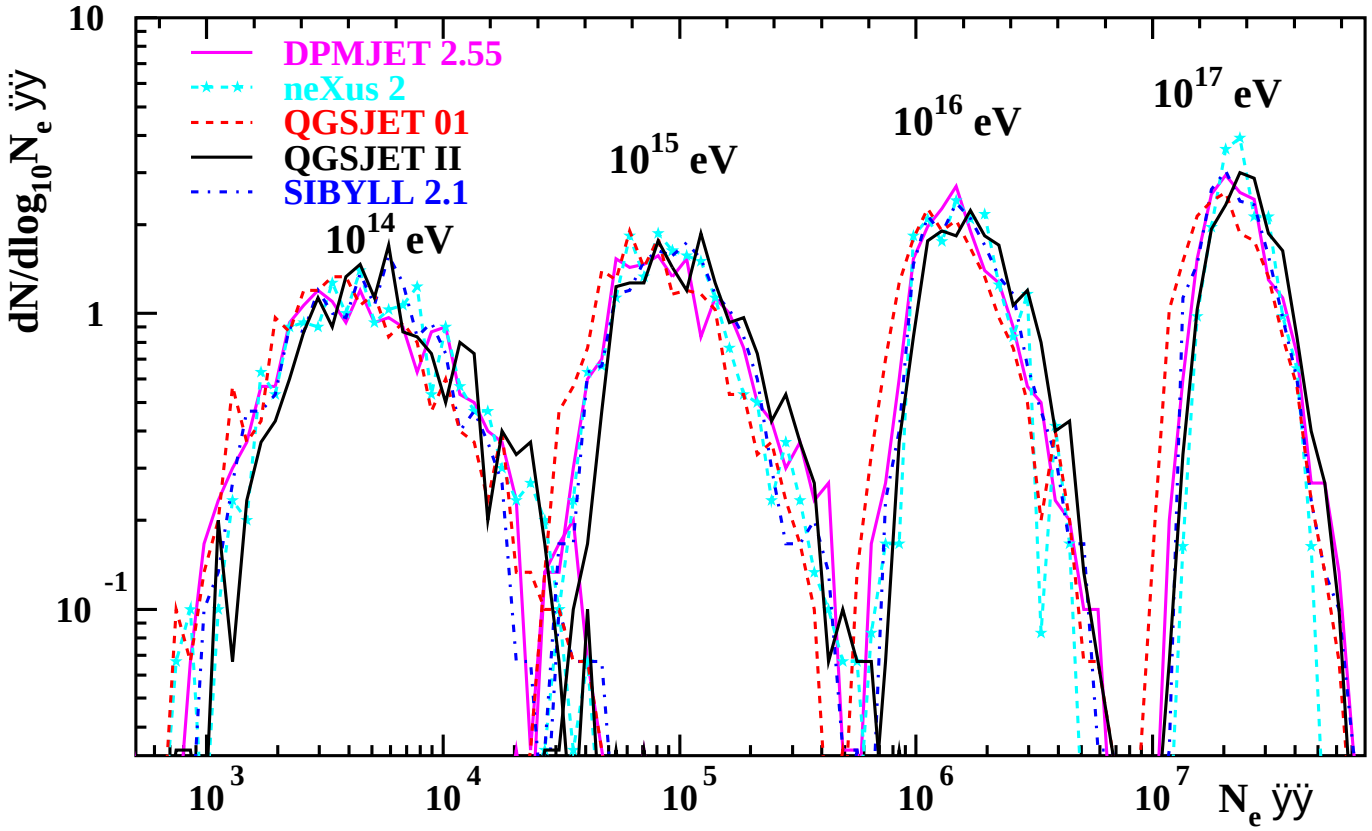

N_e–N_μ distributions for proton and iron induced vertical showers of 10^{14} to 10^{17} eV.

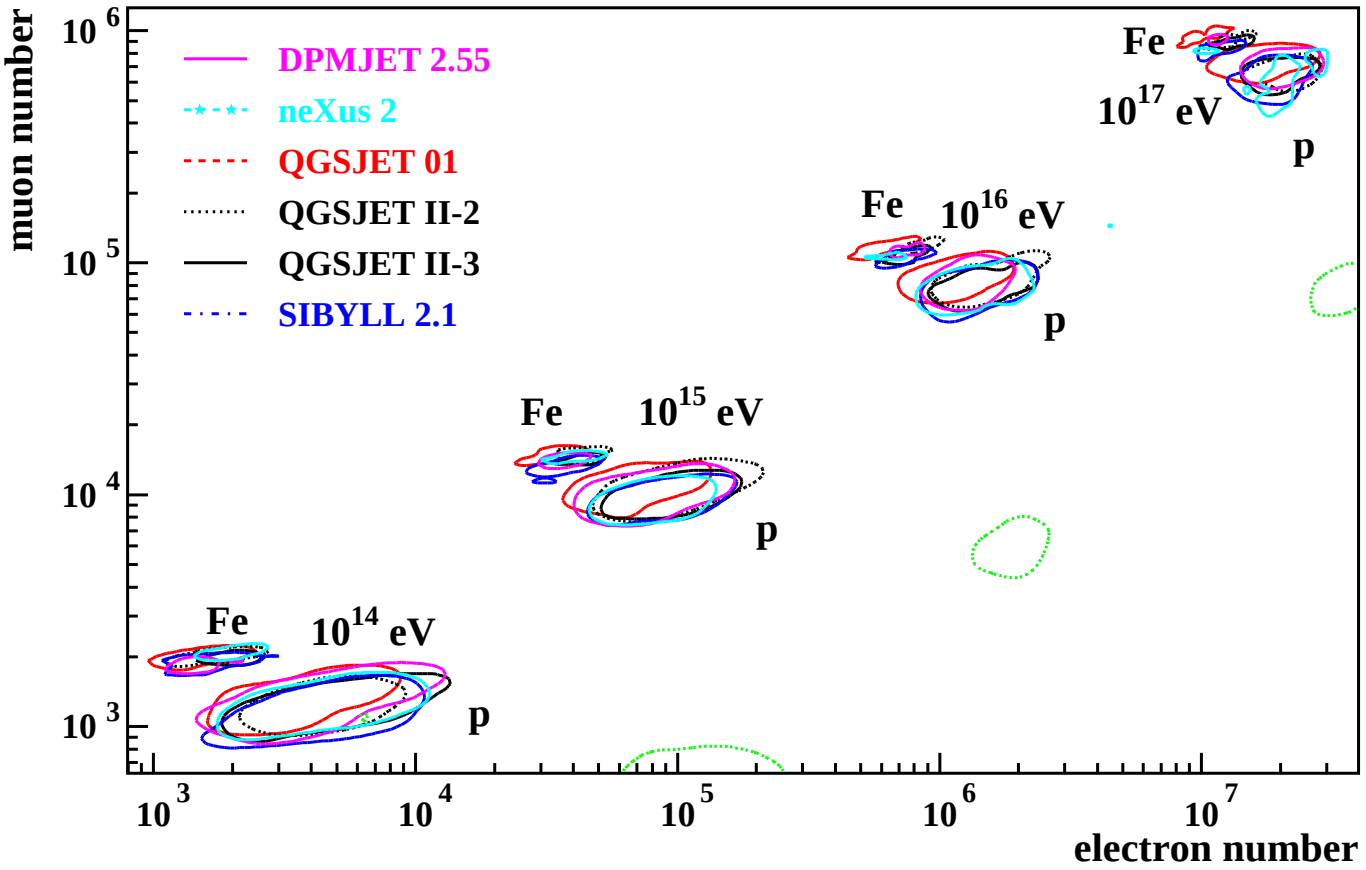

Penetration depth X_{max} for gamma, proton and iron induced vertical showers as function of the energy.

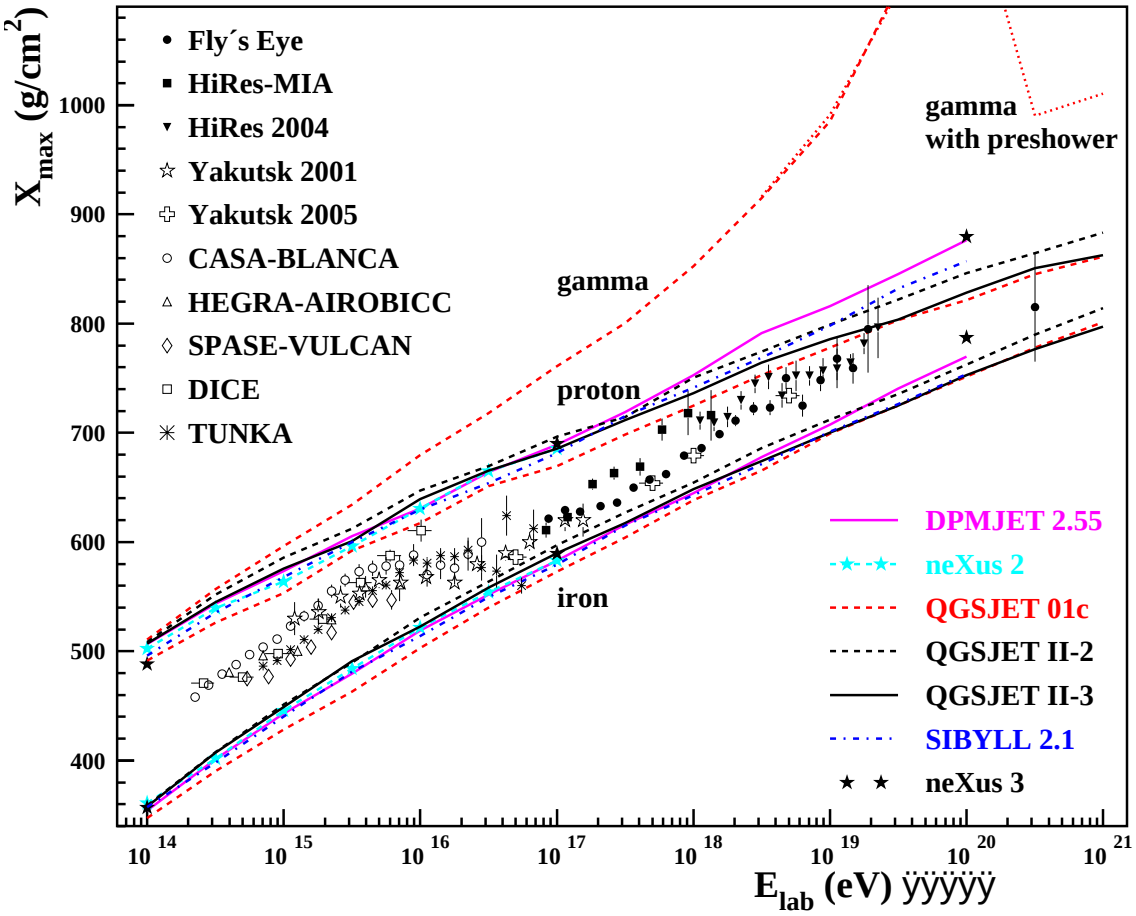

CPU–times (sec) for DEC–Alpha 1000XP

model	100000 p-Air coll 10 GeV
FLUKA	181
GHEISHA 2002	108
UrQMD 1.3	12200
model	10000 p-Air coll 1 PeV
DPMJET 2.55	271
NEXUS 2	3145
QGSJET 01	180
QGSJET II	693
SIBYLL 2.1	186

(6) Summary and conclusions

(6.1) Code comparisons

* Within 10 years of CORSIKA code comparisons: models have much improved

* Accelerator physics oriented code comparisons could help in a similar way

* include evaporation particles and residual nuclei

* compare also hadron calorimeter performance, produced and residual radioactivity

(6.2) QMD models

* Impressive performance for nucleus–nucleus collisions up to RHIC energies

* Missing: exact energy conservation, excited residual nuclei and evaporation, residual nuclei (Patches to include this into FLUKA)
  Computer running times of these models excessively long

* Construct improved relativistic model which includes all properties needed for cascades at accelerators, this could become a genuine alternative to DPM, QSM models

(6.3) DPM, QGSM models

* Impressive performance for hadron–hadron, hadron–nucleus, nucleus–nucleus, photon–hadron and photon–nucleus collisions up to present collider energies

* Improvements through CORSIKA code comparisons

* Acceptable agreement of all models up to Auger Cosmic Ray energies
  Includes also predictions for all cross sections

* These are the models which include best evaporation and residual nuclei needed for accelerator applications